Editors' Suggestion

Analytical solution for the relaxed atomic configuration of twisted bilayer graphene including heterostrain

Jian Kang [1,*] and Oskar Vafek [2,3,†]

[1] *State Key Laboratory of Quantum Functional Materials, School of Physical Science and Technology, ShanghaiTech University, Shanghai 201210, China*

[2] *National High Magnetic Field Laboratory, Tallahassee, Florida 32310, USA*

[3] *Department of Physics, Florida State University, Tallahassee, Florida 32306, USA*

(Received 6 March 2025; revised 11 August 2025; accepted 13 August 2025; published 16 September 2025)

Continuum atomic relaxation models for twisted bilayer graphene involve minimization of the sum of intralayer elastic energy and interlayer adhesion energy. The elastic energy favors a rigid twist, i.e., no distortion in the twisted honeycomb lattices, while the adhesion energy favors Bernal stacking and breaking the relaxation into triangular AB- and BA-stacked domains. We compare the results of two relaxation models with the published Bragg interferometry data, finding good agreement with one of the models. We then provide a method for finding a highly accurate approximation to the solution of this model which holds above the twist angle of $\approx 0.7^\circ$ and thus covers the first magic angle. We find closed-form expressions in the absence as well as in the presence of external heterostrain. These expressions are not written as a Taylor series in the ratio of adhesion and elastic energy because, as we show, the radius of convergence of such a series is too small to access the first magic angle.

DOI: 10.1103/s3s7-513d

I. INTRODUCTION

It became apparent fairly shortly after the discovery of correlated electron phenomena in magic-angle twisted bilayer graphene [1,2] that to explain the observed gap between the narrow and remote bands, it is necessary to model the structure of the bilayer beyond a simple rigid twist [3] and to account for atomic lattice relaxation [4–10]. The lattice relaxation originates in the difference between the energy of Bernal stacking compared with other stackings, favoring the growth of the AB- and BA-stacked regions relative to AA stacking, thus deforming the atomic configuration of the bilayer compared with the rigid twist. Such deformation results in strains within each monolayer that cost elastic energy. The relaxed configuration is understood as a result of a balance between these two effects.

More recently, it also became apparent that an unintentional external heterostrain, i.e., the layer antisymmetric component of strain, has a significant effect on the energy width of magic-angle twisted bilayer graphene narrow bands and can qualitatively modify the nature of the correlated insulator states [11,12]. Even for twist angles which, while small, are larger than the magic angle, the moire pattern magnifies the effect of strain [13]. For example, at $\sim 1.38^\circ$ twist, a $\sim 0.3\%$ heterostrain can lead to $\sim 12\%$ change in the real space moire lattice vectors. We illustrate this effect at the magic angle 1.05° in Fig. 1, showing the difference between the unstrained moire unit cell lattice vectors $\mathbf{L}_j$ and their heterostrained counterparts $\mathbf{L}'_j$. Such a large change in atomic lattice constants would be difficult to achieve in a regular material due to the limits on its stability but is readily observed in twisted bilayer graphene [14–18]. This phenomenon opens an avenue toward strain engineering the electronic properties of moire materials. For example, in Ref. [13], it was emphasized that even a small $\sim 0.2\%$ heterostrain can split the energetic degeneracy of the three Van Hove singularities in, say, the conduction moire band and introduce open Fermi surfaces within a finite energy window of the band spectrum, capable of accommodating >1 electron per moire unit cell. The magnetoresistance of the resulting electronic system with open Fermi surfaces can be very large and nonsaturating [13]. In contrast, in the absence of the external heterostrain, the Van Hove singularities are degenerate, and the window of electron filling with open Fermi surfaces shrinks to a point. For these and other reasons, we consider it important to understand the lattice relaxation in the presence of realistic heterostrain.

The purpose of this paper is to provide analytical results which can be used as an input to model the electronic properties of twisted bilayer graphene, with or without heterostrain. To have some confidence in the applicability of the theoretical model whose output is the relaxation profile, we first compare the results obtained numerically with the experimentally measured relaxation and strain profiles of twisted bilayer graphene using Bragg interferometry [18] as a function of the twist angle within the range from 0.2° to 1.4°. We do this comparison for two theoretical models, Refs. [5,10], and conclude that the results of the model from Ref. [5] follow the experiment much more closely. We therefore focus our attention on obtaining the analytical expressions for the relaxed configuration using the model of Ref. [5].

To this end, we introduce a dimensionless parameter λ that quantifies the ratio between the interlayer adhesion

*Contact author: kangjian@shanghaitech.edu.cn
†Contact author: vafek@magnet.fsu.edu

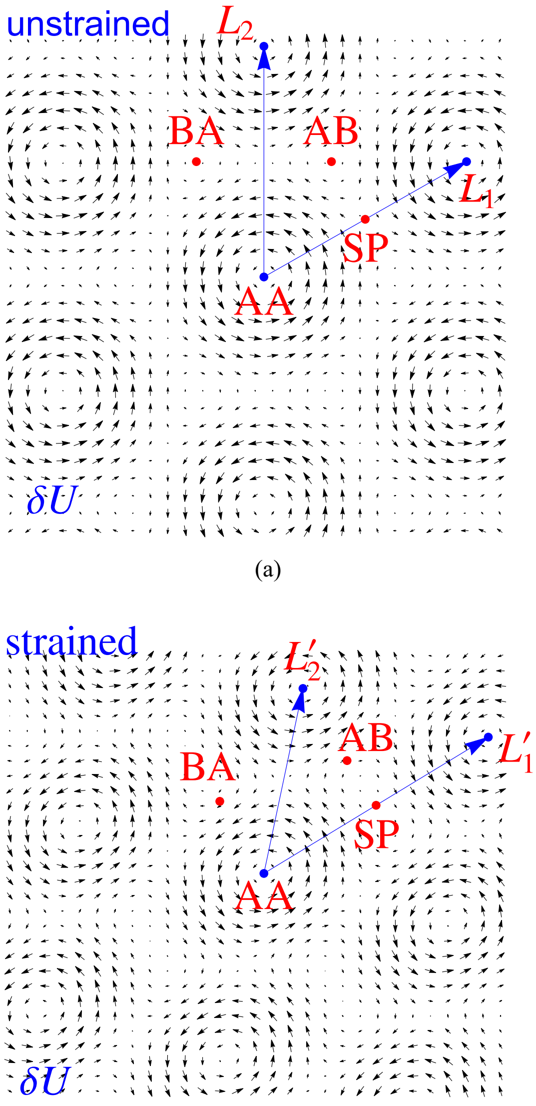

FIG. 1. Lattice relaxation for the twist angle $\theta = 1.05^\circ$ with (a) no external heterostrain and (b) $\epsilon_1 = 0.5 \times 10^{-2}$, $\epsilon_2 = -0.8\epsilon_1$, and $\phi = \pi/12$. The moire lattice vectors as well as various stacking points are also marked.

energy and the intralayer elastic energy at a given twist angle θ [it is precisely defined in Eq. (23)]. For smaller θ, λ is larger due to relative growth of the adhesion energy compared with the elastic energy and leading to a stronger lattice relaxation. At the first magic angle of $\theta \approx 1.05^\circ$, the value of λ reaches ≈ 0.256. Naively, one may expect that such a small value would allow finding the relaxed configuration by Taylor expanding it in powers of λ, an approach adopted recently in Ref. [19]. Interestingly, we find that this approach encounters shortcomings just above the first magic angle. In this regard, we can precisely show that, although the exact solution for the lattice relaxation is an analytic function of λ near the origin, the distance to the nearest point of nonanalyticity in the complex λ plane is such that the radius of convergence of the Taylor series is only ≈ 0.217. This means that including more terms in the Taylor series does not necessarily improve the accuracy of the solution near the magic angle. Instead, we introduce a different method, which allows us to obtain a simple explicit form for the relaxation as a function of λ, which is highly accurate at and below the first magic angle. This approach does not suffer from the problems encountered by the series solution method. Moreover, it can be systematically improved and extended to include external heterostrain. It is sufficiently general to allow for uniaxial and/or biaxial heterostrain that can be treated on equal footing. The analytic formulas we present are accurate to at least 1% heterostrain and thus within the range of the vast majority of the experimentally examined twisted bilayer graphene devices.

TABLE I. The elastic parameters $\mathcal{K}$ and $\mathcal{G}$ and the parameters of the interlayer adhesion potential for two models proposed in Refs. [5,10].

U_E	$\mathcal{K}$	$\mathcal{G}$	
Ref. [10]	12.82 eV/Å^2	9.57 eV/Å^2	
Ref. [5]	13.265 eV/Å^2	9.035 eV/Å^2	
U_B	c_1	c_2	c_3
Ref. [10]	3.206 meV/Å^2	0	0
Ref. [5]	0.775 meV/Å^2	−0.071 meV/Å^2	−0.018 meV/Å^2

The rest of the paper is organized as follows: In the next subsection, we summarize the main result so that the reader can readily find it without needing to go over the details of the derivation. In Sec. II, we set up the formalism to describe the twisted and strained honeycomb bilayer, review the expressions for the intralayer elastic energy and the interlayer adhesion energy, and compare the numerical solution for the relaxed configuration with the available experimental data. In Sec. II A, we present analytical formulas for the relaxed configuration in the absence of external heterostrain, while in Sec. II B, we calculate the radius of convergence of the series-expansion-in-λ solution by studying its analytic properties in the complex λ plane and finding the branch points. In Sec. III, we solve for the relaxed configuration in the presence of external heterostrain. In Sec. III A, we discuss the out-of-plane corrugation. The last section contains the discussion.

A. Summary of main results

The main result of this paper is Eq. (61), which gives a formula for the in-plane lattice relaxation of a twisted bilayer graphene subject to an external heterostrain in Eq. (4). The lattice distortion is defined via Eq. (9), the layer antisymmetric combination in Eq. (10), and Eq. (18). The three monolayer graphene reciprocal lattice vectors $\mathbf{G}_a$ are defined in Eqs. (2) and (3) and are unaffected by the strain. This is unlike the three moire reciprocal lattice vectors $\mathbf{g}_a$ in Eq. (6). The explicit formulas for the Fourier amplitudes $\zeta_{1,2,3}$ are given in Eqs. (38), (40), and (41), while the additional strain correction is given in Eq. (60), in terms of Eqs. (56)–(59). The values of the elastic constants and the adhesion energy parameters are provided in Table I.

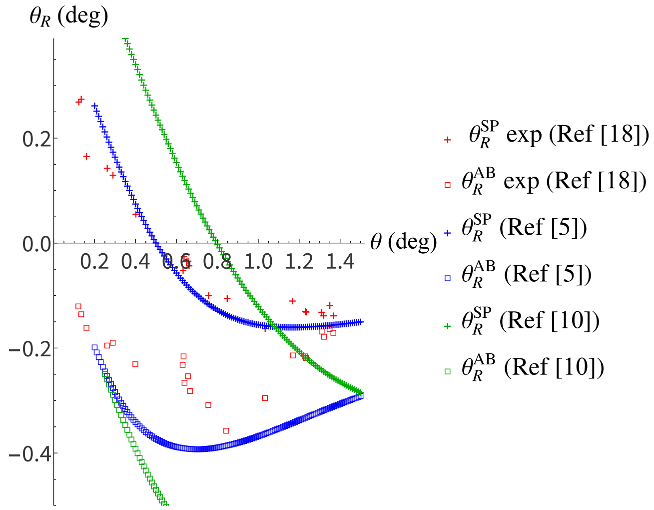

FIG. 2. $\theta_R = \frac{1}{2}(\partial_x \delta U_y - \partial_y \delta U_x)$ at two positions: SP stacking (+) at $\mathbf{x} = \frac{1}{2}\mathbf{L}_1$ and AB stacking (empty square) at $\mathbf{x} = \frac{1}{3}(\mathbf{L}_1 + \mathbf{L}_2)$, when the heterostrain is absent. The three pairs of plots show the experimental measurements (red), the results of the model in Ref. [10] (green) (see also Ref. [20]), and the results of the model in Ref. [5] (blue) (see also Ref. [20]). The experimental data are more consistent with the model in Ref. [5]. More distortion parameters are plotted and compared in Fig. 9.

II. LATTICE DISTORTION

We start by focusing on two different theoretical models for lattice relaxation proposed in Refs. [5,10] and compare the distortion obtained numerically from these two models with the experimental measurements of Ref. [18]. The experimental data cover the range of twist angle θ between 0.2° and 1.4°. As shown in Fig. 2, we find a closer match for the distortion obtained using the model in Ref. [5] than that in Ref. [10]. Therefore, in later sections, we choose the model of Ref. [5] to obtain the lattice distortion, not just numerically but also analytically.

Before proceeding with the details of the derivation, we introduce two unit cell vectors of monolayer graphene

$$\mathbf{a}_1 = a\left(-\frac{1}{2}, \frac{\sqrt{3}}{2}\right) \quad \text{and} \quad \mathbf{a}_2 = a(-1, 0), \tag{1}$$

where $a \approx 0.246$ nm is the magnitude of the monolayer graphene lattice constant. The corresponding reciprocal lattice vectors are

$$\mathbf{G}_1 = \frac{2\pi}{a}\left(0, \frac{2}{\sqrt{3}}\right), \quad \mathbf{G}_2 = -\frac{2\pi}{a}\left(1, \frac{1}{\sqrt{3}}\right). \tag{2}$$

For notational convenience, we also introduce

$$\mathbf{G}_3 = -(\mathbf{G}_1 + \mathbf{G}_2) = \frac{2\pi}{a}\left(1, -\frac{1}{\sqrt{3}}\right), \tag{3}$$

shown in Fig. 3(a).

The heterostrain is described by a 2×2 symmetric matrix S^ϵ. It can always be diagonalized by an orthogonal matrix $R(\phi)$ [7,13,15]

$$S^\epsilon = R(-\phi)\begin{pmatrix} \epsilon_1 & 0 \\ 0 & \epsilon_2 \end{pmatrix} R(\phi), \tag{4}$$

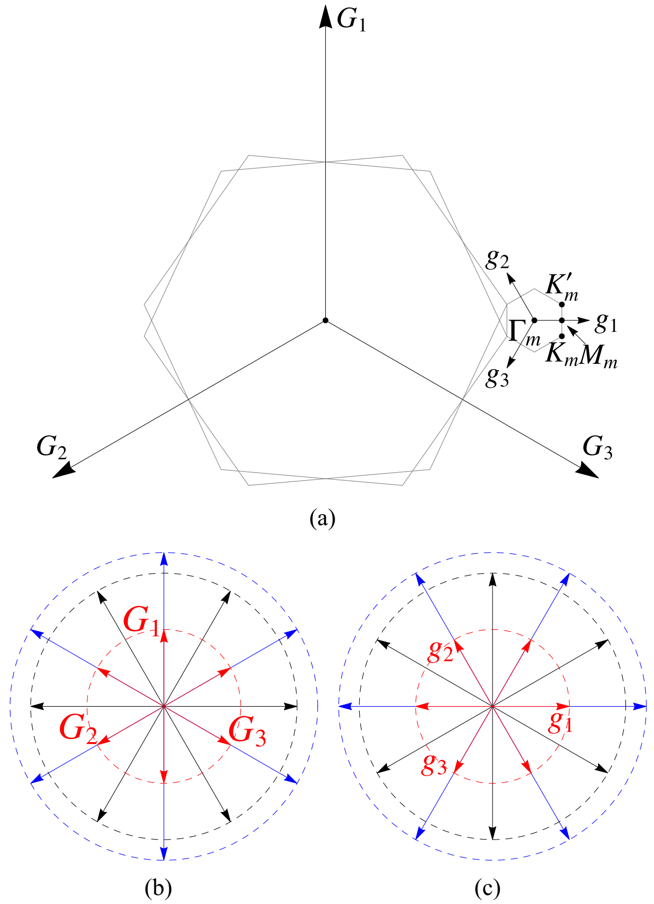

FIG. 3. (a) and (b) $\mathbf{G}_i$ are the reciprocal lattice vectors of the undistorted monolayer graphene, with $\mathbf{G}_1$, $\mathbf{G}_2$ defined by Eq. (2) and $\mathbf{G}_3 = -(\mathbf{G}_1 + \mathbf{G}_2)$. (c) $\mathbf{g}_i$ ($i = 1, 2, 3$) are the reciprocal vectors of the moire lattice given by Eq. (6); in (a) and (c), we did not include heterostrain, only the twist. (b) The first three $\mathbf{G}$-shells marked by red (the first shell), black (the second shell), and blue (the third shell) colored arrows. Note that, in our definition, the $\mathbf{G}$ vectors are unaffected by strain, unlike the $\mathbf{g}$ vectors. (c) The first three $\mathbf{g}$-shells marked by the same colored arrows as for $\mathbf{G}$-shells. Unlike in (a), in the schematics (b) and (c), we do not distinguish between different sizes of $\mathbf{G}$ and $\mathbf{g}$ vectors.

where $R(\phi) = \begin{pmatrix} \cos\phi & -\sin\phi \\ \sin\phi & \cos\phi \end{pmatrix}$ is the two-dimensional rotational matrix. Note that this rotation has nothing to do with the twist. Rather, the angle ϕ determines the orientation of the two principal axes of the strain tensor. Here, $\epsilon_{1,2}$ are the magnitudes of the strain along the two principal axes. In the case of uniaxial strain along the first principal axis, $\epsilon_2 = -\nu\epsilon_1$, where $\nu \approx 0.16$ is the Poisson ratio [7]. In this work, we also allow for the biaxial strain; therefore, both ϵ_1 and ϵ_2 are treated as external parameters, and we will not assume any specific relation between them. In the presence of experimentally relevant small twist and small heterostrain, the moire lattice vectors $\mathbf{L}_j$ and the corresponding moire reciprocal lattice vectors $\mathbf{g}_j$ can be safely expanded [7] to the linear order in the twist angle θ and $\epsilon_{1,2}$ as

$$L_{j,\mu} = (S^\epsilon - i\theta\sigma^2)^{-1}_{\mu\nu} a_{j,\nu}, \tag{5}$$

$$g_{j,\mu} = (S^\epsilon + i\theta\sigma^2)_{\mu\nu} G_{j,\nu} \quad \text{for } j = 1, 2, 3. \tag{6}$$

The Pauli matrix $i\sigma^2 = \begin{pmatrix} 0 & 1 \\ -1 & 0 \end{pmatrix}$, and S^ϵ is the strain matrix defined in Eq. (4). The full set of the moire reciprocal lattice vectors is given by

$$\mathbf{g} = n_1\mathbf{g}_1 + n_2\mathbf{g}_2, \tag{7}$$

with arbitrary integers n_1 and n_2. Note that $S^\epsilon + i\theta\sigma^2$ is a nonsingular matrix unless the strain and twist angle are fine-tuned [21]. Thus, we can set up a one-to-one mapping between the set of monolayer graphene reciprocal lattice vectors $\mathbf{G}$ and the set of $\mathbf{g}$'s as

$$g_{\mathbf{G},\mu} = (S^\epsilon + i\theta\sigma^2)_{\mu\nu}G_\nu. \tag{8}$$

We illustrate this in Figs. 3(b) and 3(c) in the absence of heterostrain for the first three shells.

As discussed in Ref. [9], under the assumptions that the lattice distortion on both layers can be approximated by a continuous function whose variation is small on the length scale of a and that the lattice distortion is independent of the graphene sublattice, we can use the Eulerian coordinates to express the distorted in-plane position $\mathbf{X}_j$, on the layer $j = t$ or b, via a continuous function of the undistorted position $\mathbf{r}$ as

$$\mathbf{X}_j = \mathbf{r} + \mathbf{U}_j(\mathbf{X}_j). \tag{9}$$

Here, $\mathbf{U}_j$ gives the distortion of the carbon atom due to the twist, strain, and relaxation. We start by considering only the (dominant) in-plane lattice relaxation and address the out-of-plane corrugation in Sec. III A. To proceed, we also introduce the layer-symmetric and layer-antisymmetric combination of the in-plane distortions

$$\mathbf{U}^+ = \tfrac{1}{2}(\mathbf{U}_t + \mathbf{U}_b), \quad \mathbf{U}^- = \mathbf{U}_t - \mathbf{U}_b. \tag{10}$$

Although first-principles approaches have been used to obtain the lattice relaxation [22–25], the vector fields $\mathbf{U}^\pm(\mathbf{x})$ can be conveniently obtained by minimizing the sum of the elastic energy U_E and the interlayer adhesion energy U_B,

$$U_{\text{tot}} = U_E + U_B, \tag{11}$$

for example, as done in Refs. [5,10,26]. The elastic energy can be expressed in terms of the sum of the layer-symmetric and layer-antisymmetric terms

$$U_E = U_E^+ + U_E^-. \tag{12}$$

The layer-antisymmetric term is a functional of $\mathbf{U}^-(\mathbf{x})$ alone

$$\begin{aligned} U_E^-[\mathbf{U}^-] = \frac{1}{4}\int \mathrm{d}^2\mathbf{x}\, \{&\mathcal{K}(\partial_x U_x^- + \partial_y U_y^-)^2 \\ &+ \mathcal{G}[(\partial_x U_x^- - \partial_y U_y^-)^2 \\ &+ (\partial_x U_y^- + \partial_y U_x^-)^2]\}, \end{aligned} \tag{13}$$

and the layer-symmetric functional U_E^+, which depends only on $\mathbf{U}^+(\mathbf{x})$, can be obtained using

$$U_E^+[\mathbf{U}^+] = 4U_E^-[\mathbf{U}^+]. \tag{14}$$

The elastic moduli $\mathcal{K}$ and $\mathcal{G}$ are listed in Table I. The interlayer adhesion term is a functional of $\mathbf{U}^-(\mathbf{x})$ alone. It is given by

$$U_B = \frac{1}{2}\sum_{\mathbf{G}} V_{\mathbf{G}} \int \mathrm{d}^2\mathbf{x}\, \cos[\mathbf{G}\cdot\mathbf{U}^-(\mathbf{x})], \tag{15}$$

where $\sum_{\mathbf{G}}$ sums over all the reciprocal lattice vectors of monolayer graphene. Note that $V_{\mathbf{G}}$ must be symmetric under various transformations, including the sixfold rotation C_{6z} and the mirror reflection about the xz plane $\mathcal{R}_y$, leading to the following constraints:

$$V_{\pm\mathbf{G}_i} = c_1, \quad V_{\pm 2\mathbf{G}_i} = c_3, \quad i = 1, 2, 3, \tag{16}$$

$$V_{\pm(\mathbf{G}_1-\mathbf{G}_2)} = V_{\pm(\mathbf{G}_2-\mathbf{G}_3)} = V_{\pm(\mathbf{G}_3-\mathbf{G}_1)} = c_2. \tag{17}$$

In most theoretical models, $V_{\mathbf{G}}$ is negligible for $|\mathbf{G}| > 2|\mathbf{G}_1|$ and thus can be safely ignored outside the first three shells. The interlayer adhesion potential parameters on the first shell c_1, second shell c_2, and third shell c_3, for two models proposed in Refs. [5,10] can be found in Table I.

Thus, $\mathbf{U}^+(\mathbf{x})$ decouples from $\mathbf{U}^-(\mathbf{x})$ (see, e.g., Ref. [9]). Therefore, minimizing U_E^+ with respect to $\mathbf{U}^+(\mathbf{x})$ leads to $\partial_x U_x^+ = \partial_y U_y^+ = 0$ and $\partial_x U_y^+ + \partial_y U_x^+ = 0$. This implies that $\mathbf{U}^+(\mathbf{x}) = \vartheta_0\hat{z}\times\mathbf{x} + \mathbf{d}_0$, where $\mathbf{d}_0$ is a constant two-component vector and ϑ_0 is a constant. Thus, $\mathbf{U}^+(\mathbf{x})$ simply represents an overall rotation of both layers by the same angle of ϑ_0 followed by an in-plane translation by the same vector $\mathbf{d}_0$. Such a transformation does not induce any change of the elastic energy and electronic spectrum (unlike the relative twist), and thus, we can safely set $\mathbf{U}^+(\mathbf{x}) = 0$.

In the presence of a twist by a small angle θ and a small external heterostrain, $\mathbf{U}^-(\mathbf{x})$ can be written as the sum of two terms

$$U_\mu^-(\mathbf{x}) = (S^\epsilon - i\theta\sigma^2)_{\mu\nu}x_\nu + \delta U_\mu(\mathbf{x}), \tag{18}$$

where the last term $\delta\mathbf{U}$ gives the lattice relaxation; S^ϵ is given by Eq. (4). For a uniform twist and external heterostrain, we seek a moire lattice periodic $\delta\mathbf{U}(\mathbf{x})$, with the lattice vectors $\mathbf{L}_i$ defined in Eq. (5), i.e., we impose the constraint $\delta\mathbf{U}(\mathbf{x}) = \delta\mathbf{U}(\mathbf{x}+\mathbf{L}_i)$ when minimizing $U_E^- + U_B$. We are thus tacitly assuming that the substrate stabilizes the flat structure and prevents the buckling transition, with bending stiffness collapse and moire translation symmetry breaking, found in the theoretical study of freestanding twisted bilayer graphene in Ref. [27]; our assumption is supported by the data of Ref. [18].

As explained in Ref. [9], the average of $\delta\mathbf{U}(\mathbf{x})$ over the space can be absorbed by redefining the origin of $\mathbf{x}$, and thus, the average can be set to 0 without loss of generality. Then both the elastic and interlayer adhesion potentials can be shown to be invariant under space inversion [9]. Although the global minima may break this symmetry, numerical calculations have not found such cases for $\theta \geqslant 0.2^\circ$ and $|\epsilon_{1,2}| < 1.5\%$. Thus, in the rest of this work, we assume that the lattice relaxation is C_{2z} odd, i.e., $\delta\mathbf{U}(\mathbf{x}) = -\delta\mathbf{U}(-\mathbf{x})$, leading to its Fourier series

$$\delta\mathbf{U}(\mathbf{x}) = \sum_{\mathbf{g}} \mathbf{W}(\mathbf{g})\sin(\mathbf{g}\cdot\mathbf{x}), \tag{19}$$

where $\sum_{\mathbf{g}}$ sums over all the moire reciprocal lattice vectors and $\mathbf{W}(\mathbf{g})$ are real and odd under $\mathbf{g}\to -\mathbf{g}$. Since Eq. (8)

constructs a one-to-one mapping between the moire reciprocal lattice vectors $\mathbf{g}$ and the reciprocal vectors $\mathbf{G}$ of the undistorted monolayer graphene lattice, it is sometimes convenient to label the Fourier components $\mathbf{W}(\mathbf{g})$ using $\mathbf{G}$ vectors. To this end, we introduce $\mathbf{W}_\mathbf{G} \equiv \mathbf{W}(\mathbf{g}_\mathbf{G})$, and the lattice relaxation will also be interchangeably written as $\delta\mathbf{U}(\mathbf{x}) = \sum_\mathbf{G} \mathbf{W}_\mathbf{G} \sin(\mathbf{g}_\mathbf{G} \cdot \mathbf{x})$.

Minimizing the sum of U_E^- and U_B leads to the self-consistent equation for $\mathbf{W}_\mathbf{G}$ (when $\mathbf{G} \neq 0$)

$$\sum_\nu M_{\mu\nu}(\mathbf{g}_\mathbf{G}) W_{\mathbf{G},\nu} = \sum_{\mathbf{G}'} V_{\mathbf{G}'} f_{\mathbf{G}'}(\mathbf{g}_\mathbf{G}, \{\mathbf{W}_\mathbf{G}\}) G'_\mu, \tag{20}$$

where $M(\mathbf{g})$ is a 2×2 matrix that can be written as

$$M_{\mu\nu}(\mathbf{g}) = \mathcal{G}|\mathbf{g}|^2 \delta_{\mu\nu} + \mathcal{K} g_\mu g_\nu, \tag{21}$$

and $f_{\mathbf{G}'}$ is the Fourier series amplitude defined via

$$\begin{aligned}\sin[\mathbf{G}' \cdot \mathbf{U}^-(\mathbf{x})] &= \sin[\mathbf{g}_{\mathbf{G}'} \cdot \mathbf{x} + \mathbf{G}' \cdot \delta\mathbf{U}(\mathbf{x})] \\ &= \sum_\mathbf{g} f_{\mathbf{G}'}(\mathbf{g}, \{\mathbf{W}_\mathbf{G}\}) \sin(\mathbf{g} \cdot \mathbf{x}). \end{aligned}\tag{22}$$

Equation (20) is a nonlinear equation that can be solved numerically by the iteration method [5,9,10,28,29]. Table I lists the parameters for two different models proposed in Refs. [5,10] that produce markedly different lattice distortions due to the significant difference in the parameter c_1. Based on these two models, we calculate their local twist $\theta_R = \frac{1}{2}(\partial_x \delta U_y - \partial_y \delta U_x)$ produced by the lattice relaxation at two positions: saddle point (SP) stacking at $\mathbf{x} = \mathbf{L}_1/2$, and AB stacking at $\mathbf{x} = \frac{1}{3}(\mathbf{L}_1 + \mathbf{L}_2)$, see Fig. 1(a), with the twist angle between 0.2° and 1.4°. The numerical results for θ_R are compared with the experimental measurements of Ref. [18] in Fig. 2. The measured θ_R at the SP follows the prediction of the model in Ref. [5] but significantly deviates from that in Ref. [10]. Although the calculation in Fig. 2 is done in the absence of an external strain, including the experimentally estimated 0.2% heterostrain when $\theta \approx 1.3°$ for either model does not result in a significant change. The agreement with the data at the AB point is also significantly better for the model of Ref. [5], although it seems to somewhat overestimate θ_R at the AB point. This disparity may be related to the experimental measurement, which inherently averages over a particular region around a special point, such as the SP, AB, or AA. Our numerical calculations shown in Fig. 2 report the lattice distortion exactly at these special points, without further averaging, and thus always produce stronger distortions than the reported measurements. Therefore, precise details of the inherent averaging in experiments would be needed to further judge the accuracy of the model in Ref. [5]. Comparisons for other distortion parameters are presented in the Appendix. Although the mentioned overestimates also occur for other distortion parameters, the overall consistency between the experiments and the model in Ref. [5] persists. In the rest of this manuscript, we will therefore focus on this lattice relaxation model.

A. Analytical formula for in-plane relaxation in the absence of external strain

We proceed to derive an approximate but accurate and simple analytical formula for $\delta\mathbf{U}$. For this purpose, it is convenient to introduce a dimensionless parameter

$$\lambda = \frac{c_1}{\mathcal{G}\theta^2} \tag{23}$$

that quantifies the ratio between the interlayer adhesion energy and the elastic energy at a given twist angle θ. For smaller θ, λ is larger, implying relative growth of the interlayer adhesion energy compared with the elastic energy and leading to stronger lattice relaxation. The theoretical model of Ref. [5] gives $\lambda \approx 0.256$ at the first magic angle of $\approx$1.05°.

In the unstrained case, the moire lattice is invariant under the sixfold rotation C_{6z} and the mirror reflections along xz and yz planes. The Helmholtz decomposition of the lattice relaxation field [9] gives

$$\delta\mathbf{U}(\mathbf{x}) = \nabla \times [\varepsilon(\mathbf{x})\hat{z}] + \nabla\varphi(\mathbf{x}), \tag{24}$$

where both fields $\varepsilon(\mathbf{x})$ and $\varphi(\mathbf{x})$ are periodic, and even under space inversion, i.e., $\varepsilon(\mathbf{x}) = \varepsilon(-\mathbf{x})$ and $\varphi(\mathbf{x}) = \varphi(-\mathbf{x})$. Thus, their Fourier series can be written as

$$\begin{aligned}\varepsilon(\mathbf{x}) = \sum_\mathbf{g} \tilde{\varepsilon}_\mathbf{g} \cos(\mathbf{g}\cdot\mathbf{x}) \quad &\text{and} \quad \varphi(\mathbf{x}) = \sum_\mathbf{g} \tilde{\varphi}_\mathbf{g} \cos(\mathbf{g}\cdot\mathbf{x}) \\ \Longrightarrow \mathbf{W}(\mathbf{g}) &= \tilde{\varepsilon}_\mathbf{g} \hat{z} \times \mathbf{g} - \tilde{\varphi}_\mathbf{g} \mathbf{g}. \end{aligned}\tag{25}$$

As mentioned, in the absence of external strain, the lattice relaxation $\delta\mathbf{U}$ is invariant under C_{6z} and odd under the mirror reflection about the xz and yz planes, leading to the symmetry constraints for both $\tilde{\varepsilon}_\mathbf{g}$ and $\tilde{\varphi}_\mathbf{g}$. As a consequence, for $\mathbf{g}$ on the first three shells, $\tilde{\varphi}_\mathbf{g}$ must vanish [19], and $\tilde{\varepsilon}_\mathbf{g}$ depends only on the shell index [9]

$$\tilde{\varepsilon}_{\pm\mathbf{g}_1} = \tilde{\varepsilon}_{\pm\mathbf{g}_2} = \tilde{\varepsilon}_{\pm\mathbf{g}_3} = \frac{\zeta_1}{\theta|\mathbf{G}_1|^2}, \tag{26}$$

$$\tilde{\varepsilon}_{\pm(\mathbf{g}_1-\mathbf{g}_2)} = \tilde{\varepsilon}_{\pm(\mathbf{g}_2-\mathbf{g}_3)} = \tilde{\varepsilon}_{\pm(\mathbf{g}_3-\mathbf{g}_1)} = \frac{\zeta_2}{\theta|\mathbf{G}_1|^2}, \tag{27}$$

$$\tilde{\varepsilon}_{\pm2\mathbf{g}_1} = \tilde{\varepsilon}_{\pm2\mathbf{g}_2} = \tilde{\varepsilon}_{\pm2\mathbf{g}_3} = \frac{\zeta_3}{\theta|\mathbf{G}_1|^2}. \tag{28}$$

In the above, we introduced the dimensionless parameters ζ_i ($i = 1$, 2, and 3) which quantify the strength of $\mathbf{W}(\mathbf{g})$ on the ith shell as $|\mathbf{W}(\mathbf{g})|/a \sim |\mathbf{g}|\tilde{\varepsilon}_\mathbf{g}/a \sim |\mathbf{g}|\zeta_i/(\theta|\mathbf{G}_1|^2 a) \sim \zeta_i$. Explicitly displaying the Fourier amplitudes on the first three shells, the lattice distortion field has the form

$$\begin{aligned}\delta\mathbf{U}(\mathbf{x}) = &\frac{2}{|\mathbf{G}_1|^2} \sum_{a=1}^{3} \mathbf{G}_a[\zeta_1 \sin(\mathbf{g}_a\cdot\mathbf{x}) + 2\zeta_3 \sin(2\mathbf{g}_a\cdot\mathbf{x})] \\ &+ \frac{2\zeta_2}{|\mathbf{G}_1|^2} \sum_{a=1}^{3} (\mathbf{G}_a - \mathbf{G}_{a+1}) \sin[(\mathbf{g}_a - \mathbf{g}_{a+1})\cdot\mathbf{x}] \\ &+ \dots, \end{aligned}\tag{29}$$

where for notational simplicity, we define $\mathbf{G}_4 = \mathbf{G}_1$ and $\mathbf{g}_4 = \mathbf{g}_1$, $|\mathbf{G}_1| = 4\pi/(\sqrt{3}a)$, and … stands for terms at higher shells than the third.

The solution to Eq. (20) in the absence of the interlayer adhesion term U_B is simple, namely, $\delta\mathbf{U} = 0$. Therefore, when the adhesion term is small compared with the elastic term, we expect $\mathbf{W}(\mathbf{g})$ to be small as well. Assume that we have found this solution. We then extract its amplitude on the first shell $\pm\mathbf{g}_{1,2,3}$ and express it in terms of ζ_1. We can then estimate the magnitudes of the solution on the higher $\mathbf{g}$ shells ζ_2, ζ_3, etc., in terms of ζ_1. We see that, for small λ and given the hierarchy $|c_1| \gg |c_{2,3}|$ in Table I, the solution for $\zeta_{2,3}$ is down by a factor of either $c_{2,3}/c_1$ or λ compared with ζ_1. The suppression is even stronger on further shells. Therefore, $\delta\mathbf{U}$ is almost entirely determined by the Fourier amplitudes on the innermost shell. By solving Eq. (20) numerically using the iteration method, the full solution (which we have at each shell) confirms that, for $\theta \gtrsim 0.7^\circ$, the Fourier series of $\delta\mathbf{U}(\mathbf{x})$ is indeed dominated by the innermost shell.

Since $\mathbf{W}(\mathbf{g})$ is small on the outer shells for the twist angles of interest to us, the Fourier components on the outer shells have a negligible impact on the innermost shell. Consequently, ζ_1 can be obtained accurately by setting $\zeta_2 = \zeta_3 = 0$ in Eq. (29), ignoring the higher shells denoted by the ellipsis, and then minimizing $U_E^- + U_B$. Explicitly, we start by setting

$$\delta\mathbf{U}(\mathbf{x}) \rightarrow \frac{2\zeta_1}{|\mathbf{G}_1|^2}\sum_{j=1}^{3}\mathbf{G}_j \sin(\mathbf{g}_j\cdot\mathbf{x}), \tag{30}$$

substituting the above into Eq. (13), and obtaining

$$\frac{U_E^-}{A_{\text{tot}}} = \frac{3\mathcal{G}\theta^2\zeta_1^2}{2}, \tag{31}$$

where A_{tot} is the total area of the sample. We see that the elastic energy does not depend on the elastic coefficient $\mathcal{K}$ because $\delta\mathbf{U}(\mathbf{x})$ on the first $\mathbf{g}$-shell is divergence free. The elastic energy cost also grows as a square of the twist angle because the moire period decreases inversely as the twist angle increases, and the moire period sets the scale of the spatial variation penalized by the elastic energy. The interlayer adhesion energy U_B in Eq. (15) can be written as

$$\frac{U_B}{A_{\text{tot}}} = A_{\text{tot}}^{-1}\sum_{\mathbf{G}} V_{\mathbf{G}} \int d^2\mathbf{x} \times \frac{1}{4}\{\exp(i\mathbf{g}_{\mathbf{G}}\cdot\mathbf{x})\exp[i\mathbf{G}\cdot\delta\mathbf{U}(\mathbf{x})] + \text{c.c.}\}. \tag{32}$$

To perform the Fourier integral, we note that the phase factor associated with the distorted configuration is periodic and can be expanded via Fourier series as [30]

$$\begin{aligned}\exp[i\mathbf{G}\cdot\delta\mathbf{U}(\mathbf{x})] &= \prod_{j=1}^{3}\exp[2i\sin(\mathbf{g}_j\cdot\mathbf{x})\mathbf{G}\cdot\mathbf{W}(\mathbf{g}_j)] \\ &= \sum_{n_1=-\infty}^{\infty}\sum_{n_2=-\infty}^{\infty}\sum_{n_3=-\infty}^{\infty}\left[\prod_{j=1}^{3}J_{n_j}\left(2\zeta_1\frac{\mathbf{G}\cdot\mathbf{G}_j}{|\mathbf{G}_1|^2}\right)\right]\exp\left[i\left(\sum_{j=1}^{3}n_j\mathbf{g}_j\right)\cdot\mathbf{x}\right],\end{aligned} \tag{33}$$

where $J_n(x)$ is the Bessel function of the first kind (with integer n). Substituting the above into Eq. (32), we obtain

$$\begin{aligned}\frac{U_B}{A_{\text{tot}}} &= \frac{1}{2}\sum_{\mathbf{G}} V_{\mathbf{G}}\sum_{n_1,n_2,n_3=-\infty}^{\infty}\left[\prod_{j=1}^{3}J_{n_j}\left(2\zeta_1\frac{\mathbf{G}\cdot\mathbf{G}_j}{|\mathbf{G}_1|^2}\right)\right]\delta_{\mathbf{g}_{\mathbf{G}}+\sum_{j=1}^{3}n_j\mathbf{g}_j,0} \\ &= 3c_2[J_1(3\zeta_1)]^2 + 3\sum_{n=-\infty}^{\infty}\left\{c_1J_n(2\zeta_1)[J_{n+1}(\zeta_1)]^2 + c_3J_n(4\zeta_1)[J_{n+2}(2\zeta_1)]^2\right\}.\end{aligned} \tag{34}$$

The last equality has been derived by noting that $V_{\mathbf{G}} \neq 0$ if and only if $\mathbf{G}$ is located on the first three shells.

By minimizing $U_E^- + U_B$ with respect to ζ_1, we obtain

$$0 = \zeta_1 + \lambda\frac{d}{d\zeta_1}\left(\frac{c_2}{c_1}[J_1(3\zeta_1)]^2 + \sum_{n=-\infty}^{\infty}\left\{J_n(2\zeta_1)[J_{n+1}(\zeta_1)]^2 + \frac{c_3}{c_1}J_n(4\zeta_1)[J_{n+2}(2\zeta_1)]^2\right\}\right). \tag{35}$$

Using $dJ_n(x)/dx = \frac{1}{2}[J_{n-1}(x) - J_{n+1}(x)]$, one can obtain a numerical solution of the above equation which will give the optimal ζ_1 in terms of λ; we did so, and because we find a highly accurate closed-form solution below which matches this numerical solution, we do not show it in Fig. 4.

To proceed analytically, we first note that, as $\lambda \rightarrow 0$, the above equation is satisfied if $\zeta_1 \rightarrow 0$. Physically, this is the limit of the short moire period when the elastic energy cost of relaxation dominates the interlayer adhesion energy gain, and the in-plane relaxation vanishes. Therefore, as we increase λ and ζ_1 increases from zero, we can approximate the right-hand side of Eq. (35) by Taylor expanding it in small ζ_1, noting that the Bessel functions of the first kind $J_n(z)$, with integer n, are entire functions of complex z. This is justified if the solution for ζ_1 we seek remains small. We find that, for $0 \leqslant \lambda \lesssim 0.44$, an accurate solution can be obtained by Taylor expanding the right-hand side of Eq. (35) in ζ_1 to second order, giving

$$0 \approx 3\lambda\zeta_1^2 + (1 + \alpha\lambda)\zeta_1 - \lambda, \tag{36}$$

where for notational convenience, we introduced the parameter

$$\alpha = \frac{1}{2} + \frac{9}{2}\frac{c_2}{c_1} + 4\frac{c_3}{c_1}. \tag{37}$$

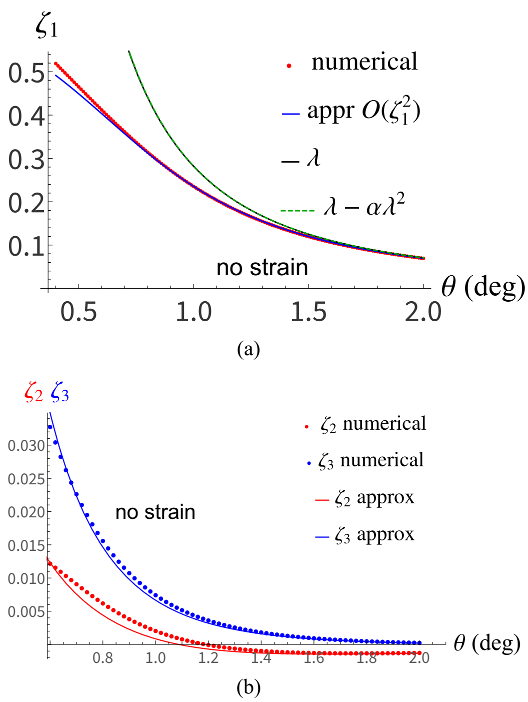

FIG. 4. The numerical solution [20] to Eq. (20), minimizing the sum of the elastic energy U_E and the interlayer adhesion energy U_B, is obtained first; it includes many **g**-shells and achieves convergence. (a) Red dots show the amplitude of this solution at the first shell $\pm\mathbf{g}_{1,2,3}$ for the parameters of Ref. [5] in Table I, expressed in terms of the dimensionless variable ζ_1 [see Eq. (29)]. The blue curve is the approximate formula given in Eq. (38) using our approach, upon which we can systematically improve, as explained in the main text. The solid black and dashed green curves are the Taylor expansions of the solution to the first and second orders in the dimensionless parameter $\lambda = c_1/(\mathcal{G}\theta^2)$ that quantifies the relative magnitudes of U_B and U_E at a given twist angle θ. The Taylor expansions are seen to be accurate above the twist angle $\sim 1.6^\circ$ but to increasingly deviate below. In Sec. II B, we explain the poor performance of the Taylor series expansion by finding its radius of convergence, which translates to the twist angle 1.14°, and placing the magic angle beyond the reach of the Taylor expansion approach. (b) Dots show the analogous numerical results at the second and third shells, demonstrating that, in this range of twist angles, the dimensionless amplitudes $\zeta_{2,3}$ are at least an order of magnitude smaller than ζ_1. The solid lines are our approximate formulas; next-order improvements can be found in the Fig. 11.

Solving the quadratic Eq. (36) gives us an accurate analytical formula for the optimal amplitude on the first **g** shell

$$\zeta_1 \approx \frac{1}{6\lambda}\left[-(1+\alpha\lambda) + \sqrt{(1+\alpha\lambda)^2 + 12\lambda^2}\right]. \tag{38}$$

With the parameters listed in Table I for Ref. [5], we can obtain a numerical solution of Eq. (20). We then extract the corresponding ζ_j for the relaxation on the jth **g**-shell using $\zeta_j = \frac{|\mathbf{g}_1|^2}{|\mathbf{g}|^2}\mathbf{G}_\mathbf{g}\cdot\mathbf{W}(\mathbf{g})$, where $\mathbf{G}_g = \hat{z}\times\mathbf{g}/\theta$ and **g** is on the jth shell. The comparison of such a numerical result on the first shell with the approximate formula in Eq. (38) is presented in Fig. 4, showing excellent agreement for the twist angle θ down to at least 0.7°.

The closed-form expressions for ζ_2 and ζ_3 for the second and third shells can be obtained using similar methods. Starting from Eq. (29) with ζ_1 from Eq. (38), we keep ζ_1 fixed and expand the total energy $U_E^- + U_B$ up to the quadratic order of ζ_2 and ζ_3. This approximation for the energy is justified since ζ_2 and ζ_3 are $\ll 1$ for the twist angle θ down to 0.2°, notably smaller than the first magic angle. Integrating Eq. (13) over the space, we found the exact formula for the elastic energy

$$\frac{U_E^-}{A_{\text{tot}}} = \frac{3}{2}\mathcal{G}\theta^2\left(\zeta_1^2 + 9\zeta_2^2 + 16\zeta_3^2\right). \tag{39}$$

We also obtain a (complicated) formula for U_B that is presented in the Appendix. Minimizing $U_E^- + U_B$ and expanding the Bessel functions to $O(\zeta_1^2)$, we obtain the approximate solutions for ζ_2 and ζ_3

$$\zeta_2 \approx \frac{\lambda}{6}\zeta_1 + \frac{\lambda}{3}\frac{c_2}{c_1} - \frac{\lambda}{6}\zeta_1\left(\zeta_1 + 4\frac{c_3}{c_1}\right), \tag{40}$$

$$\zeta_3 \approx \frac{\lambda}{8}\zeta_1 + \frac{\lambda}{4}\frac{c_3}{c_1}. \tag{41}$$

Figure 4(b) shows the plots of ζ_2 and ζ_3 with parameters specified in Table I for the model proposed in Ref. [5]. Clearly, the analytical formulas in Eqs. (40) and (41) match the full numerical solution very well for $\theta \gtrsim 0.7^\circ$. In addition, when $\lambda \ll 1$ (as is the case for $\theta \gtrsim 1^\circ$), then $\zeta_1 \approx \lambda$, as seen from Eq. (38), and $\zeta_2/\zeta_1 \sim \zeta_3/\zeta_1 \sim \max(\lambda, |c_2|/c_1) \ll 1$, confirming our *a priori* estimates. Therefore, the Fourier components of the distortion on the outer shells are much smaller than on the first shell, as also confirmed in Fig. 4. This hierarchy in the lattice relaxation not only justifies the assumption when deriving Eqs. (40) and (41) but also allows us to neglect the impact of outer-shell relaxation on the electronic Hamiltonian for $\theta \gtrsim 1^\circ$, as will be shown in an upcoming paper.

We thus obtain a highly accurate expression for the difference between the in-plane layer displacements in the two layers $\mathbf{U}^- = \mathbf{U}_t - \mathbf{U}_b$. The accuracy of our formulas for ζ_i can be further improved, as explicitly worked out in Appendix C.

B. Radius of convergence for the lattice relaxation

To compare with the results of Refs. [19,30], we expand our solution in Eq. (38) in a power series of λ, finding $\zeta_1 \approx \lambda - \alpha\lambda^2 + O(\lambda^3)$. Although we do not rely on such power-series expansion, and in fact discuss its shortcomings below, we note that our leading term $\zeta_1 \approx \lambda$ agrees with the $O(\lambda)$ result obtained in Refs. [19,30] provided we identify $c_1/(2\sin^2\frac{\theta}{2})$ and $2\alpha_1$ of the latter with our λ and ζ_1, respectively. Expanding to such a low order agrees with the full numerical solution on the first **g**-shell for $\theta \gtrsim 1.6^\circ$ but increasingly overestimates the relaxation at smaller angles; the deviation is $\sim 20\%$ at the (first) magic angle. Our prefactor of λ^2 also agrees with the $O(\lambda^2)$ prefactor in Ref. [19] provided $c_2 = c_3 = 0$, in which case $\alpha = 0.5$. This prefactor is significantly corrected by nonzero c_2 and c_3, as shown in Eq. (37), and the resulting prefactor $\alpha \approx -0.0076$ is tiny for the model proposed in Ref. [5].

Our closed-form solution allows us to understand the convergence of the power-series expansion in λ by studying the analytic properties in the complex λ plane. The solution in Eq. (38) contains a branch cut with branch points at $\lambda_{\text{BP}} =$

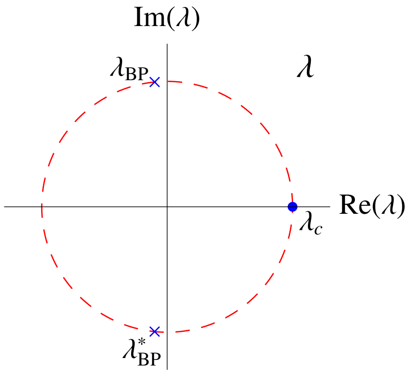

FIG. 5. Schematic plot for the branch points of the function $\zeta_1(\lambda)$ in the complex λ-plane, whose magnitude $|\lambda_{\rm BP}|$ dictates the radius of convergence λ_c of the power-series expansion of $\zeta_1(\lambda)$ about $\lambda = 0$. Note that the two branch points, marked by the blue crosses, are complex conjugates of each other.

$(-\alpha + 2\sqrt{3}i)/(\alpha^2 + 12)$ and $\lambda^*_{\rm BP}$. A complex circle centered at the origin and passing through the branch points intersects the real λ axis at $\lambda_c = 1/\sqrt{12+\alpha^2}$, as shown in Fig. 5; λ_c is the radius of convergence of the power series [31]. As a consequence, the power expansion of Eq. (38) in λ must diverge if $\lambda > \lambda_c$. With the parameters of Ref. [5] specified in Table I, we obtain $\lambda_c \simeq 0.289$ with the corresponding angle $\theta_c = 0.99^\circ$. Note that our solution in Eq. (38) is perfectly smooth at $\lambda_c = |\lambda_{\rm BP}|$, and the singularity occurs only in the power expansion.

Because the right-hand side of Eq. (35) is an analytic function of ζ_1 and λ, we can also study its zeros in the complex λ plane numerically without approximating the right-hand side by a quadratic polynomial in ζ_1. For a fixed complex value of λ, the zeros of the real part form curves in the complex ζ_1 plane, as do the zeros of the imaginary part. Their intersection gives the solutions of Eq. (35), the physical one being on the real ζ_1 axis for real λ and vanishing with vanishing λ. For $c_2 = c_3 = 0$, we find that two solutions closest to the origin are $\lambda_{\rm BP} = \lambda_c \exp(\pm i\pi\delta)$ with machine precision $\lambda_c = 0.2603353755476081$ and $\delta = 0.5568038282560424$ (see Appendix B for the method to obtain these and for the proof of the existence of the branch points). These correspond to the branch points we found approximately using Eq. (38). For the values of c_2 and c_3 listed in Table I for Ref. [5], we find $\lambda_c = 0.2166638106379033$ and $\delta = 0.4681651233626292$, further reducing the radius of convergence of any power series in the λ solution to the amplitude of the first **g**-shell of $\delta\mathbf{U}(\mathbf{x})$. This value of λ_c translates to the twist angle $\theta_c = 1.14^\circ$, placing the first magic angle just outside the radius of convergence and making the power-series approach impractical for obtaining an increasingly accurate solution near the first magic angle. As mentioned, our closed-form solution does not suffer from this problem. We can further improve upon it by expanding the right-hand side of Eq. (35) to the third order in ζ_1 and solving the corresponding cubic equation for ζ_1 in terms of λ. We have done so, but because the expressions are somewhat unwieldy and Eq. (38) is sufficiently accurate for our purposes down to and below the first magic angle, we do not write out the solution of the cubic here.

III. LATTICE RELAXATION IN THE PRESENCE OF AN EXTERNAL HETEROSTRAIN

Having discussed the lattice relaxation in the unstrained twisted bilayer, we study the impact of the external heterostrain that is described by a 2×2 symmetric matrix shown in Eq. (4). Although the heterostrain is ubiquitous in realistic twisted samples, the two strain parameters ϵ_1 and ϵ_2 are always much smaller than the twist angle θ, in which case the matrix $S^\epsilon + i\theta\sigma^2$ introduced in Eq. (8) is nonsingular. As a consequence, the lattice relaxation $\delta\mathbf{U}(\mathbf{x})$ is still periodic, and its periods are given by two noncollinear moire lattice vectors $\mathbf{L}_1$ and $\mathbf{L}_2$ defined in Eq. (5). The strained lattice relaxation is obtained by solving Eq. (20) with the corresponding moire reciprocal lattice vectors **g** given in Eq. (6).

Even with the approximation scheme used in the previous section for the unstrained case, it is hopelessly challenging to obtain a closed-form solution of Eq. (20) without making any further assumptions about the magnitude of the heterostrain. Nevertheless, we can make progress by using the fact that, in realistic devices, the external heterostrain is small, i.e., $|\epsilon_{1,2}| \ll \theta$. This can be used to derive an approximate but closed-form solution for the change of lattice relaxation due to external heterostrain. To this end, we express the lattice relaxation as

$$\delta\mathbf{U}(\mathbf{x}) = 2\sum_{\mathbf{G}\in\mathbb{H}} \mathbf{W}_{\mathbf{G}} \sin(\mathbf{g}_{\mathbf{G}} \cdot \mathbf{x}), \tag{42}$$

where $\mathbf{g}_{\mathbf{G}}$'s are the heterostrain-distorted moire reciprocal lattice vectors defined in Eq. (8), and we introduced $\mathbb{H}$ to be half of the set of nonzero **G** vectors, which includes one and only one vector for each nonzero vector pair $(\mathbf{G}, -\mathbf{G})$. This can be done because $\mathbf{g}_{\mathbf{G}}$ is linear in **G**, and $\mathbf{W}_{\mathbf{G}}$ is odd under $\mathbf{G} \to -\mathbf{G}$, as discussed below Eq. (19). The geometric effect of heterostrain on the reciprocal lattice vectors in Eq. (8) can be isolated as

$$\mathbf{g}_{\mathbf{G}} = \mathbf{g}^{(0)}_{\mathbf{G}} + \delta\mathbf{g}_{\mathbf{G}} \quad \text{with} \tag{43}$$

$$g^{(0)}_{\mathbf{G},\mu} = \theta i\sigma^2_{\mu\nu} G_\nu \quad \text{and} \quad \delta g_{\mathbf{G},\mu} = S^\epsilon_{\mu\nu} G_\nu. \tag{44}$$

In addition, we decompose $\mathbf{W}_{\mathbf{G}}$ into two parts

$$\mathbf{W}_{\mathbf{G}} = \mathbf{W}^{(0)}_{\mathbf{G}} + \delta\mathbf{W}_{\mathbf{G}}, \tag{45}$$

where $\mathbf{W}^{(0)}_{\mathbf{G}}$ is the solution of Eq. (20) in the absence of external heterostrain. It has already been determined in the previous section: For **G** on the first three shells,

$$\mathbf{W}^{(0)}_{\mathbf{G}\in j\text{th shell}} = \zeta_j \frac{\mathbf{G}}{|\mathbf{G}_1|^2}, \quad j = 1, 2, 3, \tag{46}$$

while for $j > 3$, $\mathbf{W}^{(0)}_{\mathbf{G}}$ is too small and thus can be neglected. Here, $\delta\mathbf{W}_{\mathbf{G}}$ gives the heterostrain-induced change of the Fourier coefficients of the lattice relaxation $\delta\mathbf{U}(\mathbf{x})$, at the reciprocal lattice vectors $\mathbf{g}_{\mathbf{G}}$. Note that these reciprocal lattice vectors are themselves modified by the heterostrain, as shown in Eq. (43).

The equation for $\delta\mathbf{W}_{\mathbf{G}}$ is obtained by substituting Eqs. (43) and (45) into Eq. (20). To present its explicit form, we first decompose the matrix introduced in Eq. (21) into three parts, organized by the powers of $\delta\mathbf{g}$,

$$M(\mathbf{g}_\mathbf{G}) = M^{(0)}_\mathbf{G} + M^{(1)}_\mathbf{G} + M^{(2)}_\mathbf{G}, \tag{47}$$

$$M^{(0)}_{\mathbf{G},\mu\nu} = \mathcal{G}\big|\mathbf{g}^{(0)}_\mathbf{G}\big|^2\delta_{\mu\nu} + \mathcal{K}g^{(0)}_{\mathbf{G},\mu}g^{(0)}_{\mathbf{G},\nu}, \tag{48}$$

$$M^{(1)}_{\mathbf{G},\mu\nu} = 2\mathcal{G}\big[\mathbf{g}^{(0)}_\mathbf{G}\cdot\delta\mathbf{g}_\mathbf{G}\big]\delta_{\mu\nu} + \mathcal{K}\big[g^{(0)}_{\mathbf{G},\mu}\delta g_{\mathbf{G},\nu} + \delta g_{\mathbf{G},\mu}g^{(0)}_{\mathbf{G},\nu}\big], \tag{49}$$

$$M^{(2)}_{\mathbf{G},\mu\nu} = \mathcal{G}|\delta\mathbf{g}_\mathbf{G}|^2\delta_{\mu\nu} + \mathcal{K}\delta g_{\mathbf{G},\mu}\delta g_{\mathbf{G},\nu}. \tag{50}$$

Then as explicitly derived in the Appendix, Eq. (20) results in the following equation for $\delta\mathbf{W}$:

$$0 = \big[M^{(0)}_\mathbf{G} + M^{(1)}_\mathbf{G} + M^{(2)}_\mathbf{G}\big]_{\mu\nu}\big[\mathbf{W}^{(0)}_\mathbf{G} + \delta\mathbf{W}_\mathbf{G}\big]_\nu + \frac{\partial}{\partial W_{\mathbf{G},\mu}}\frac{1}{2}\sum_{\mathbf{G}'}V_{\mathbf{G}'}B(\mathbf{G}',\{\mathbf{W}\})\bigg|_{\mathbf{W}=\mathbf{W}^{(0)}+\delta\mathbf{W}}. \tag{51}$$

In the above, we introduced the function $B(\mathbf{G},\{\mathbf{W}\})$ which is most easily defined via a Fourier integral as

$$B(\mathbf{G},\{W\}) = \frac{1}{A_{\text{tot}}}\int d^2\mathbf{x}\ \exp(i\mathbf{g}_\mathbf{G}\cdot\mathbf{x}) \times \prod_{\mathbf{G}'\in\mathbb{H}}\left[\sum_{n=-\infty}^{\infty}J_n(2\mathbf{G}\cdot\mathbf{W}_{\mathbf{G}'})\exp(in\mathbf{g}_{\mathbf{G}'}\cdot\mathbf{x})\right]. \tag{52}$$

Here, $J_n(x)$ is the Bessel function of the first kind, and the set $\mathbb{H}$ is introduced in Eq. (42). Of course, the above integral can be performed analytically, but we find it more transparent to present it this way.

So far, no approximations have been made, and the obtained nonlinear equation for $\delta\mathbf{W}$ is still difficult to solve. However, $\delta\mathbf{W}$ must vanish in the absence of strain. Therefore, for $|\epsilon_{1,2}| \ll \theta \ll 1$, we expect $|\delta\mathbf{W}| \ll |\mathbf{W}^{(0)}|$, leading to $|\mathbf{G}\cdot\delta\mathbf{W}_{\mathbf{G}'}| \ll |\mathbf{G}\cdot\mathbf{W}^{(0)}_{\mathbf{G}'}| \lesssim \zeta_1 \sim \lambda \lesssim 1$. As a consequence, the last term in Eq. (51) needs to be known only near the solution $\delta\mathbf{W}$, which we argue is small for small heterostrain. Therefore, the complicated nonlinear term can be approximated by Taylor series in powers of $\delta\mathbf{W}$. Expanding it up to the linear order in $\mathbf{G}\cdot\delta\mathbf{W}$ leads to a set of coupled linear equations for $\delta\mathbf{W}$. Since $\mathbf{W}^{(0)}$ is the solution for the unstrained case, Eq. (51) holds when $\delta\mathbf{g} = \delta\mathbf{W} = 0$. The coupled linear equations can be expressed as

$$0 = \sum_\nu\big[M^{(1)}_\mathbf{G} + M^{(2)}_\mathbf{G}\big]_{\mu\nu}W^{(0)}_{\mathbf{G},\nu} + \sum_\nu\big[M^{(0)}_\mathbf{G} + M^{(1)}_\mathbf{G} + M^{(2)}_\mathbf{G}\big]_{\mu\nu}\delta W_{\mathbf{G},\nu} + \sum_{\mathbf{G}',\nu}[T(\{\mathbf{W}^{(0)}\})]_{\mathbf{G},\mu,\mathbf{G}',\nu}\delta W_{\mathbf{G}',\nu}, \tag{53}$$

where for notational convenience, we introduced $T(\{\mathbf{W}^{(0)}\})$ defined as

$$[T(\{\mathbf{W}^{(0)}\})]_{\mathbf{G},\mu,\mathbf{G}',\nu} = \sum_{\mathbf{G}''}\frac{V_{\mathbf{G}''}}{2}\frac{\partial^2 B(\mathbf{G}'',\ \{\mathbf{W}\})}{\partial W_{\mathbf{G},\mu}\partial W_{\mathbf{G}',\nu}}\bigg|_{\mathbf{W}=\mathbf{W}^{(0)}}. \tag{54}$$

Note that the first term in Eq. (53) is a constant, independent of $\delta\mathbf{W}$, and the last two terms are linearly proportional to $\delta\mathbf{W}$. Therefore, we have successfully transformed the nonlinear Eq. (51) into a linear equation for $\delta\mathbf{W}$. However, due to the infinite number of $\mathbf{G}$ vectors, the T matrix is also of infinite size and thus needs to be truncated to be practical and to allow obtaining $\delta\mathbf{W}$. In the Appendix, we present a detailed argument showing that $\delta\mathbf{W}_\mathbf{G}$ is much larger for $\mathbf{G}$ on the first shell than on further shells, allowing us to neglect all $\delta\mathbf{W}_\mathbf{G}$'s except $\delta\mathbf{W}_{\mathbf{G}_a}$ ($a = 1$, 2, and 3) in Eq. (53). Thus, we obtain the reduced form of Eq. (53)

$$\sum_{b=1}^{3}\sum_{\nu=1}^{2}(\mathcal{M}+\mathcal{T})_{a\mu,b\nu}\delta W_{\mathbf{G}_b\nu} = -u_{a\mu}, \tag{55}$$

where the reduced form of the first term in Eq. (53), entering the right-hand side of the above equation, can be expressed via the heterostrain-distorted reciprocal moire lattice vectors $\mathbf{g}_a$ in Eq. (6), the reciprocal moire vectors in the absence of the heterostrain $\mathbf{g}^{(0)}_a$, as well as their difference $\delta\mathbf{g}_a = \mathbf{g}_a - \mathbf{g}^{(0)}_a$, as

$$u_{a\mu} = \frac{\zeta_1}{|\mathbf{G}_1|^2}\Big\{\mathcal{G}\big[|\mathbf{g}_a|^2 - \big|\mathbf{g}^{(0)}_a\big|^2\big]G_{a,\mu} + \mathcal{K}(\delta\mathbf{g}_a\cdot\mathbf{G}_a)g_{a,\mu}\Big\}. \tag{56}$$

The block diagonal 6×6 matrix $\mathcal{M}$ in Eq. (55) can also be conveniently expressed in terms of $\mathbf{g}_a$'s and the elastic coefficients $\mathcal{G}$ and $\mathcal{K}$ as

$$\mathcal{M}_{a\mu,b\nu} = \delta_{ab}(\mathcal{G}|\mathbf{g}_a|^2\delta_{\mu\nu} + \mathcal{K}g_{a,\mu}g_{a,\nu}). \tag{57}$$

Although the matrix $\mathcal{T}$ with its elements defined as $\mathcal{T}_{a\mu,b\nu} = [T(\{\mathbf{W}^{(0)}\})]_{\mathbf{G}_a,\mu,\mathbf{G}_b,\nu}$ is independent of the external heterostrain, its expression is still quite complicated because of the formally infinite products of infinite sums of Bessel functions. Therefore, further approximations need to be made to the $\mathcal{T}$ matrix elements to obtain the closed-form expression for $\delta\mathbf{W}$. Because the unstrained solution is dominated by the first shell, we keep only $\mathbf{W}^{(0)}_{\mathbf{G}_a} = \zeta_1\mathbf{G}_a/|\mathbf{G}_1|^2$ and set all other $\mathbf{W}^{(0)}_\mathbf{G}$'s to zero. This turns every element of the 6×6 matrix $\mathcal{T}$ into a nonlinear function of ζ_1 alone. Next, we expand these nonlinear functions up to the order ζ_1^2. This effectively truncates the infinite product onto only the first shell of $\mathbb{H}$ as well as turns the infinite sum into a finite sum over a manageable number of terms, leading to closed-form expressions for the diagonal blocks $\mathcal{T}_{a\mu,a\nu}$ and the off-diagonal blocks $\mathcal{T}_{a\mu,b\nu}$ ($a \neq b$)

$$\mathcal{T}_{a\mu,a\nu} = c_1\left[\left(3\zeta_1 - \frac{9}{8}\zeta_1^2\right)|\mathbf{G}_1|^2\delta_{\mu\nu} + \left(\zeta_1 + \frac{\zeta_1^2}{2}\right)G_{a,\mu}G_{a,\nu}\right] + 4c_3G_{a,\mu}G_{a,\nu}, \tag{58}$$

$$\mathcal{T}_{a\mu,b\nu} = c_1\left[\left(1+\zeta_1-\frac{7}{4}\zeta_1^2\right)G_{c,\mu}G_{c,\nu} - \frac{3}{2}\zeta_1\left(1-\frac{\zeta_1}{2}\right)|\mathbf{G}_1|^2\delta_{\mu\nu}\right] + 6c_3\zeta_1(|\mathbf{G}_1|^2\delta_{\mu\nu} - 2G_{c,\mu}G_{c,\nu})$$
$$- c_2\left\{(\mathbf{G}_a-\mathbf{G}_b)_\mu(\mathbf{G}_a-\mathbf{G}_b)_\nu + \frac{3}{2}\zeta_1\left[\frac{9}{2}|\mathbf{G}_1|^2\delta_{\mu\nu} - (\mathbf{G}_a-\mathbf{G}_b)_\mu(\mathbf{G}_a-\mathbf{G}_b)_\nu\right]\right\} \quad \text{with} \quad a \neq b. \tag{59}$$

For convenience, here, we introduce the notation $\mathbf{G}_c = -(\mathbf{G}_a + \mathbf{G}_b)$ when $a \neq b$, with no sum over repeated indices. As a result, $\delta\mathbf{W}_{\mathbf{G}_a}$ can be solved simply by inverting the 6×6 matrix $\mathcal{M}+\mathcal{T}$, which can always be done analytically using the cofactor method. Thus,

$$\delta W_{\mathbf{G}_a,\mu} = -\sum_{b=1}^{3}\sum_{\nu=1}^{2}(\mathcal{M}+\mathcal{T})^{-1}_{a\mu,b\nu}u_{b\nu}, \tag{60}$$

and the heterostrained lattice relaxation can be accurately approximated as

$$\delta\mathbf{U}(\mathbf{x}) \approx 2\sum_{a=1}^{3}\left\{\left(\frac{\zeta_1\mathbf{G}_a}{|\mathbf{G}_1|^2}+\delta\mathbf{W}_{\mathbf{G}_a}\right)\sin(\mathbf{g}_a\cdot\mathbf{x}) + \frac{\zeta_2(\mathbf{G}_a-\mathbf{G}_{a+1})}{|\mathbf{G}_1|^2}\sin[(\mathbf{g}_a-\mathbf{g}_{a+1})\cdot\mathbf{x}] + \frac{2\zeta_3\mathbf{G}_a}{|\mathbf{G}_1|^2}\sin(2\mathbf{g}_a\cdot\mathbf{x})\right\}, \tag{61}$$

where $\mathbf{G}_4 = \mathbf{G}_1$ and $\mathbf{g}_4 = \mathbf{g}_1$, and $|\mathbf{G}_1| = 4\pi/(\sqrt{3}a)$. Recall that $\mathbf{g}_a$'s are the heterostrain-distorted reciprocal moire lattice vectors in Eq. (6), while $\mathbf{G}_a$'s are unaffected by heterostrain [see Eqs. (2) and (3)]. If we only keep the first shell, i.e., set $\zeta_2 = \zeta_3 = 0$, and use ζ_1 from Eq. (38), then the above result is accurate to within 4% for $\theta \gtrsim 1^\circ$ and, as we will show in an upcoming paper, can be safely used to obtain the electronic spectrum (see also Refs. [32,33]). Higher accuracy can be achieved by including ζ_2 and ζ_3 from Eqs. (40) and (41), respectively, allowing us to go below the first magic angle with high accuracy even at $\sim 0.7^\circ$. Figure 6(a) compares the full numerical solution for $\delta\mathbf{W}$ and our analytical solution in Eq. (60) for a particular form of the strain matrix S^ϵ with $\phi = 0$ and $\epsilon_2 = -0.16\epsilon_1$. As can be seen, the agreement between the two is very good all the way up to $\epsilon_1 \approx 0.01 = 1\%$ or $\epsilon_1/\theta \lesssim 0.55$.

Although Eq. (60) provides a closed-form expression for the heterostrain-induced correction to the relaxed atomic configuration, it involves an inverse of the 6×6 matrix which is cumbersome to express in a simple analytical form. We can further simplify it by noting that there is a hierarchy between the sizes of the matrix $\mathcal{M}$—which is simple to invert because it is block diagonal and effectively involves only 2×2 matrices—and the matrix $\mathcal{T}$. Namely, $|\mathcal{T}_{a\mu,b\nu}|/|\mathcal{M}_{c\rho,c\sigma}| \lesssim c_1|\mathbf{G}_1|^2/\mathcal{G}|\mathbf{g}_1|^2 \sim \lambda$. Therefore, when $\lambda \ll 1$, the inverse of the matrix $\mathcal{M}+\mathcal{T}$ can be Taylor expanded as

$$(\mathcal{M}+\mathcal{T})^{-1} = \mathcal{M}^{-1} - \mathcal{M}^{-1}\mathcal{T}\mathcal{M}^{-1} + \mathcal{M}^{-1}\mathcal{T}\mathcal{M}^{-1}\mathcal{T}\mathcal{M}^{-1} + \dots, \tag{62}$$

where $\mathcal{M}^{-1}$ can be explicitly expressed as

$$(\mathcal{M}^{-1})_{a\mu,b\nu} = \delta_{ab}\left(\frac{\delta_{\mu\nu}}{\mathcal{G}|\mathbf{g}_a|^2} - \frac{\mathcal{K}g_{a,\mu}g_{a,\nu}}{\mathcal{G}(\mathcal{G}+\mathcal{K})|\mathbf{g}_a|^4}\right). \tag{63}$$

The power series in Eq. (62) can be truncated at any order to produce an approximate closed-form expression for $(\mathcal{M}+\mathcal{T})^{-1}$. The accuracy of the truncation order depends on the value of λ. For $\theta \gtrsim 1.4^\circ$ or equivalently $\lambda \lesssim 0.1$, the truncation at zeroth order is highly accurate, as shown in Fig. 7, leading to

$$\delta W_{\mathbf{G}_a,\mu} \approx -\sum_\nu(\mathcal{M})^{-1}_{a\mu,a\nu}u_{a,\nu} = \frac{\zeta_1}{|\mathbf{G}_1|^2}\left\{\left[\frac{|\mathbf{g}_1^{(0)}|^2}{|\mathbf{g}_a|^2}-1\right]G_{a,\mu} - \frac{\mathcal{K}}{\mathcal{G}+\mathcal{K}}\frac{|\mathbf{g}_a^{(0)}|^2}{|\mathbf{g}_a|^4}(\delta\mathbf{g}_a\cdot\mathbf{G}_a)g_{a,\mu}\right\}. \tag{64}$$

At the first magic angle, the accuracy of different higher-order-in-$\mathcal{T}$ truncation orders is illustrated in Fig. 8, where they are compared with the full numerical solution of Eq. (20) as a function of the strain orientation angle ϕ for different values of ϵ_1.

A. Lattice corrugation

In addition to the in-plane relaxation, the atoms of twisted bilayer graphene also deform along the out-of-plane direction. Such deformation is described by the lattice corrugation field, defined as

$$h(\mathbf{x})\hat{z} = \mathbf{U}_t^\perp(\mathbf{x}) - \mathbf{U}_b^\perp(\mathbf{x}), \tag{65}$$

where $\mathbf{U}_j^\perp$ is the lattice distortion on the layer j along the out-of-plane direction. Here, $h(\mathbf{x})$ is determined by the local interlayer stacking, achieving the maximum h_{AA} at AA stacking and the minimum h_{AB} at AB stacking [34].

The interlayer stacking is given by the relative in-plane distortion $\mathbf{U}^-$. For AA stacking, $\mathbf{U}^- = n_1\mathbf{a}_1 + n_2\mathbf{a}_2$, where $n_{1,2}$ are two arbitrary integers and $\mathbf{a}_{1,2}$, as defined in Eq. (1), are the monolayer graphene lattice vectors. For AB/BA stacking, $\mathbf{U}^- = (n_1 \pm \frac{1}{3})\mathbf{a}_1 + (n_2 \pm \frac{1}{3})\mathbf{a}_2$. It is straightforward to write the corrugation field h as a function of the position $\mathbf{x}$, as has been done in Eq. (65). However, it is more convenient to express h as a function of $\mathbf{U}^-$, i.e., $h = h(\mathbf{U}^-)$, because of its dependence on the interlayer stacking. In the rest of this section, we consider various symmetries which constrain the form of $h(\mathbf{U}^-)$ and obtain its approximate formula.

The corrugation field h depends on the local interlayer stacking that does not change under the shift $\mathbf{U}^-(\mathbf{x}) \to \mathbf{U}^-(\mathbf{x}) + \mathbf{a}_j$ (with $j = 1, 2$). Therefore, $h(\mathbf{U}^-)$ is a periodic function $h(\mathbf{U}^-) = h(\mathbf{U}^- + \mathbf{a}_j)$ that can be expressed via

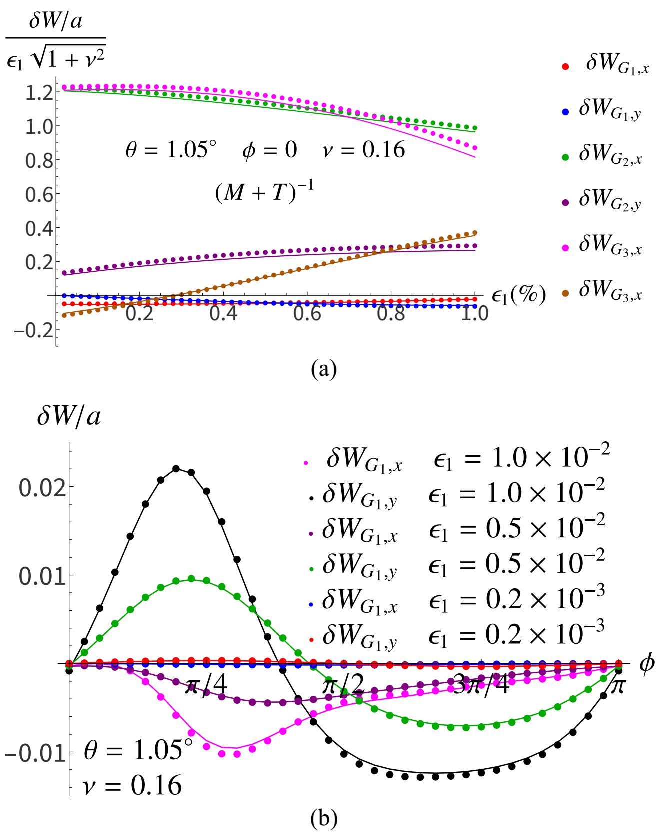

FIG. 6. The heterostrain-induced change of the Fourier amplitudes of the relaxation field, labeled by $\delta\mathbf{W}_\mathbf{G}$ and defined in Eq. (45) [see also Eqs. (42), (18), (10), and (9)] is divided by the graphene lattice constant $a \approx 0.246$ nm and plotted as a function of (a) ϵ_1 and (b) ϕ, the two parameters entering S^ϵ introduced in Eq. (4). The plots were obtained at the magic angle with $\theta = 1.05^\circ$. The remaining strain parameter is set to $\epsilon_2 = -\nu\epsilon_1$ using the Poisson ratio $\nu = 0.16$. Only $\delta\mathbf{W}_\mathbf{G}$ with $\mathbf{G}$ at the first shell is sizable; other $\delta\mathbf{W}_\mathbf{G}$'s are negligible for realistic samples. (a) Colored dots illustrate the direct numerical solution [20] of Eq. (20) resulting in δW vs ϵ_1 (with $\phi = 0$), with each component marked by different colors. Because $\delta\mathbf{W}$ grows with increasing heterostrain, we rescaled it by the magnitude of the strain matrix, defined as $\sqrt{\mathrm{Tr}((S^\epsilon)^2)} = |\epsilon_1|\sqrt{1+\nu^2}$. The solutions obtained using the simple set of six linear equations in Eq. (55) are also presented as colored curves for comparison, showing excellent agreement with the full numerical calculation even when ϵ_1 is as large as 1%. (b) The two components of $\delta\mathbf{W}_{\mathbf{G}_1}$ vs ϕ (at different ϵ_1) as obtained by (colored dots) numerically solving Eq. (20) and (colored curves) by solving Eq. (55). Again, these two approaches produce solutions in excellent agreement. Although only $\delta\mathbf{W}_{\mathbf{G}_1}$ is plotted here, $\delta\mathbf{W}_{\mathbf{G}_2}$ and $\delta\mathbf{W}_{\mathbf{G}_3}$ can also be obtained from $\delta\mathbf{W}_{\mathbf{G}_1}$ from the symmetry constraints as listed in Eqs. (E8) and (E9).

Fourier series as

$$h(\mathbf{U}^-) = \sum_{\mathbf{G}} h_\mathbf{G} \exp(i\mathbf{G}\cdot\mathbf{U}^-). \tag{66}$$

If the interlayer stacking is also invariant under C_{6z} and mirror reflections along xz and yz planes, then the Fourier components $h_\mathbf{G}$ are also unchanged under these transformations. Specifically, $h_\mathbf{G}$ is identical at each of the six $\mathbf{G}$'s on the first shell. Note that $h = h_{\mathrm{AA}}$ for AA stacking and $h = h_{\mathrm{AB}}$ for AB stacking. Approximating $h(\mathbf{U}^-)$ by keeping $h_\mathbf{G}$ in Eq. (66) only at $\mathbf{G} = 0$ and the first shell, i.e., at $|\mathbf{G}| \leqslant |\mathbf{G}_1|$, we obtain [6]

$$h(\mathbf{x}) = \frac{1}{3}(h_{\mathrm{AA}} + 2h_{\mathrm{AB}}) + \frac{2}{9}(h_{\mathrm{AA}} - h_{\mathrm{AB}})\sum_{a=1}^{3}\cos[\mathbf{G}_a\cdot\mathbf{U}^-(\mathbf{x})], \tag{67}$$

where the layer-antisymmetric in-plane distortion $\mathbf{U}^-$ is given by Eq. (18).

IV. SUMMARY

In this work, we have compared the lattice relaxation from two models in Refs. [5,10] with the experimental results obtained in Ref. [18] and found that the latter model (Ref. [5]) follows the experimental data much more closely. Using this model, we then derived a closed-form expression for the lattice relaxation. In the absence of external heterostrain, we found our analytical expression for the lattice relaxation is highly accurate for the twist angles down to ~0.7°. Introducing the dimensionless parameter λ that quantifies the ratio between the interlayer adhesion energy and the elastic energy at a given twist angle, we also found that, when the lattice relaxation is expanded in the Taylor series in λ, it becomes divergent at a value of λ which translates to the twist angle slightly above the magic value for realistic models of elastic energy and interlayer adhesion energy. We related this divergence to the existence of the branch points of the solution in the complex λ plane and numerically determined the radius of convergence of the Taylor series with high precision.

We also derived a closed-form expression for the strain-induced change of the lattice relaxation. This formula is accurate at least up to 1% heterostrain. It can be used to understand the electronic spectrum of the twisted bilayer graphene in the presence of realistic heterostrain. Incorporating these results into the electronic continuum model will be a subject of an upcoming paper.

ACKNOWLEDGMENTS

J.K. acknowledges support from the NSFC Grant No. 12074276, the Double First-Class Initiative Fund of ShanghaiTech University, and the start-up grant of ShanghaiTech University. O.V. was funded in part by the Gordon and Betty Moore Foundation's EPiQS Initiative Grant No. GBMF11070 and acknowledges support from the National High Magnetic Field Laboratory funded by the National Science Foundation (Grant No. DMR-2128556) and the State of Florida.

DATA AVAILABILITY

The data that support the findings of this article are openly available [20].

APPENDIX A: COMPARISON WITH THE EXPERIMENTS

In this section, we compare the experiments reporting the lattice relaxation with the calculated relaxation from two different theoretical models proposed in Refs. [5,10]. Instead

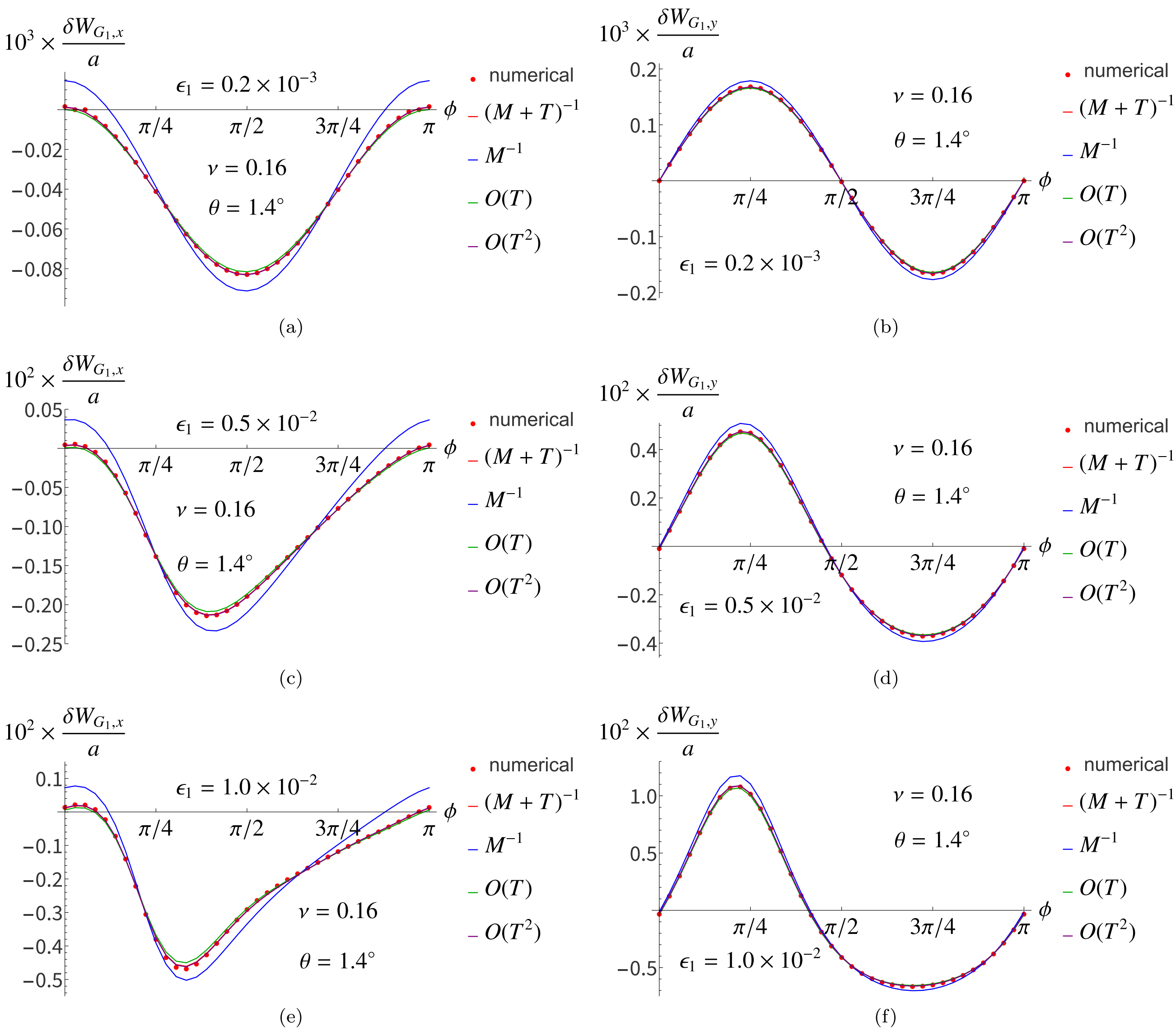

FIG. 7. Like Fig. 8, we plot $\delta \mathbf{W}_{\mathbf{G}_1}$ as a function of ϕ for the twist angle $\theta = 1.4°$. The truncation at $O(\mathcal{T})$ is almost identical to $(\mathcal{M}+\mathcal{T})^{-1}$. Compared with $\lambda \approx 0.256$ at $\theta = 1.05°$ and the truncation order at $O(\mathcal{T}^2)$, smaller $\lambda \approx 0.1$ at $\theta = 1.4°$ leads to lower truncation order of the power series expansion in Eq. (62).

of using the closed-form solution for lattice relaxation, we numerically solve the self-consistent equation [Eq. (20)] using the iteration method to obtain the lattice relaxation for these two theoretical models.

Figure 2 illustrates the relaxation-induced twist, defined as $\theta_R = \frac{1}{2}(\partial_x \delta U_y - \partial_y \delta U_x)$, at the SP and AB-stacking point, for both the experiment and the calculation from two theoretical models. The experimental measurement is more consistent with the model proposed in Ref. [5]. As a consequence, this model is chosen to derive the closed form of the lattice relaxation with and without external heterostrain. In addition, this model is used in upcoming works to study the electronic continuum model and the strain-induced change of the electron spectrum. In this section, we compare other quantities of the relaxation at high-symmetry points. Based on the comparison of these quantities, the same conclusion is drawn that the model proposed in Ref. [5] is more consistent with the experimental measurements.

The derivative of the lattice relaxation is a rank-2 tensor $\epsilon_{\mu\nu}(\mathbf{x}) = \partial_\mu \delta U_\nu$ that contains four independent components. The antisymmetric part gives the local twist $\theta_R = \frac{1}{2}(\epsilon_{xy} - \epsilon_{yx})$ as defined in the main text. The symmetric part $M^s_{\mu\nu}(\mathbf{x}) = \frac{1}{2}(\epsilon_{\mu\nu} + \epsilon_{\nu\mu})$ contains three independent parameters and can be diagonalized by an orthogonal matrix

$$M^s(\mathbf{x}) = R^T[\phi'(\mathbf{x})]\begin{bmatrix} \epsilon_{\max}(\mathbf{x}) & 0 \\ 0 & \epsilon_{\min}(\mathbf{x}) \end{bmatrix} R[\phi'(\mathbf{x})], \tag{A1}$$

where $R(\phi')$ is the 2×2 matrix describing the rotation along the $\hat{z}$ axis with the rotation angle of ϕ', and $\epsilon_{\max}$ and $\epsilon_{\min}$ are the magnitudes of strain along two principle axes. Note that all the parameters $\epsilon_{\max}$, $\epsilon_{\min}$, and ϕ' are position dependent.

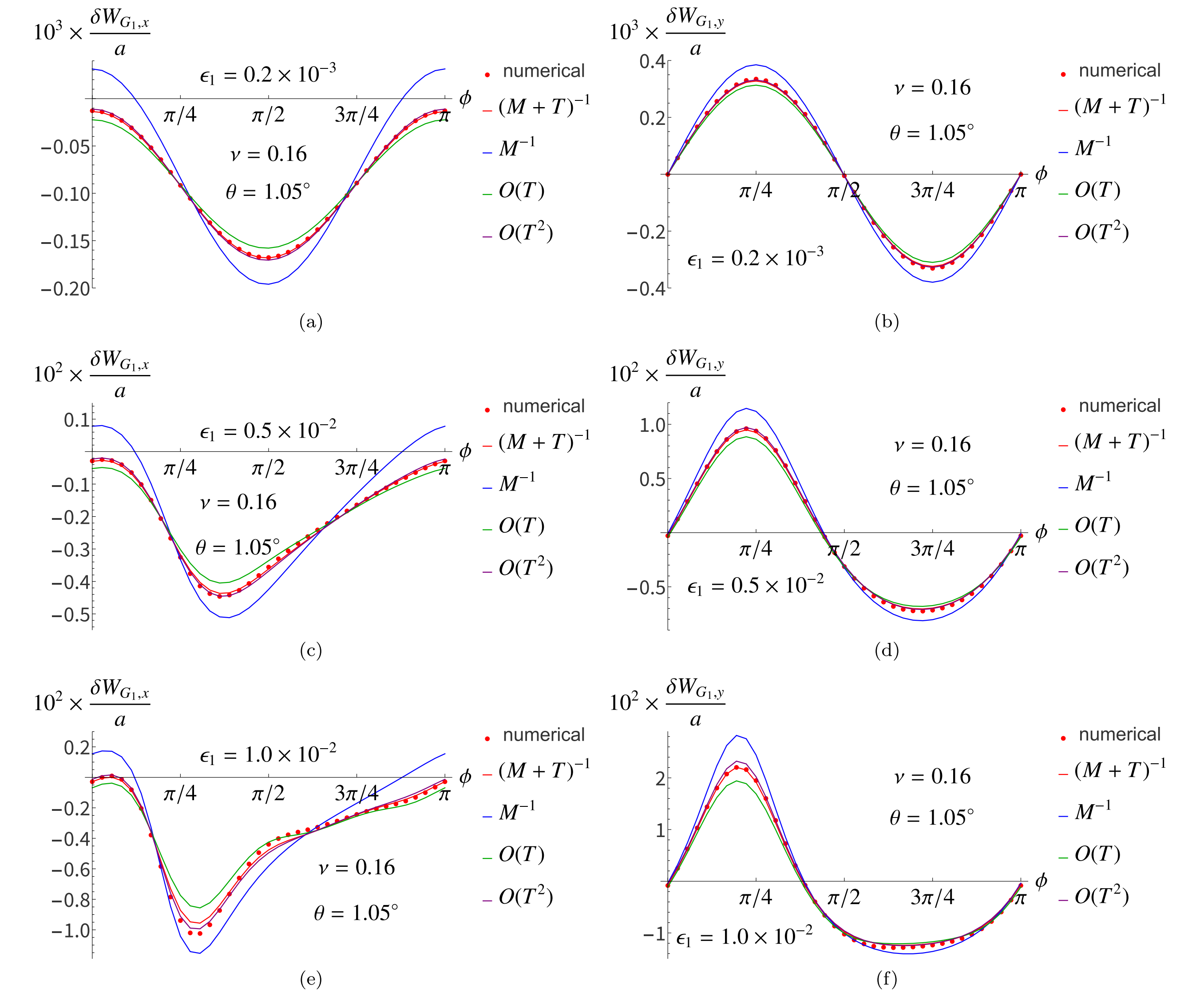

FIG. 8. Like Fig. 6(b), the x (left) and y (right) components of $\delta\mathbf{W}_{\mathbf{G}_1}$ vs ϕ, at the first magic angle $\theta = 1.05°$, with $\epsilon_1 = 0.02\%$ (first row), $\epsilon_1 = 0.5\%$ (second row), and $\epsilon_1 = 1\%$ (third row). The remaining strain parameter is set to $\epsilon_2 = -\nu\epsilon_1$ using the Poisson ratio $\nu = 0.16$. Red dots illustrate $\delta\mathbf{W}$ obtained by numerically solving Eq. (20) [20]. The solid red curves are the solutions obtained from Eq. (60). Other colored curves give $\delta\mathbf{W}$ obtained by truncating $(\mathcal{M}+\mathcal{T})^{-1}$ in Eq. (60) at different orders of $\mathcal{T}$ in the power-series expansion [see Eq. (62)], showing that the truncation at $O(\mathcal{T}^2)$ is almost identical to $(\mathcal{M}+\mathcal{T})^{-1}$.

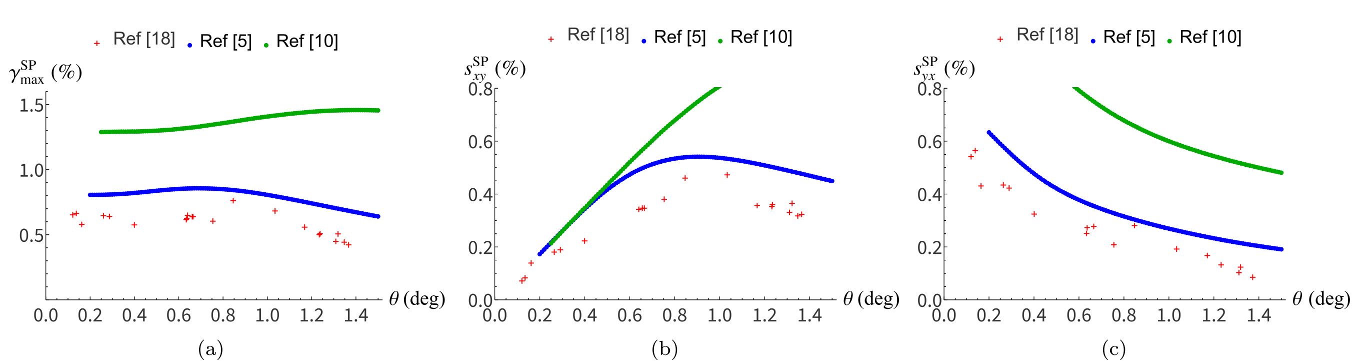

FIG. 9. Various relaxation parameters of (a) $\gamma_{\max}$, (b) s_{xy}, and (c) s_{yx} at SP stacking ($\mathbf{x} = \frac{1}{2}\mathbf{L}_1$) when the heterostrain is absent. Three different datasets are included: the experimental measurements (red), the calculation of the model proposed in Ref. [10] (green), and the calculation of the model proposed in Ref. [5] (blue). The experimental measurements are more consistent with the model proposed in Ref. [5].

In addition to $\theta_R(\mathbf{x})$, in Ref. [18], several quantities have been introduced to describe the lattice relaxation

$$\gamma_{\max} = \epsilon_{\max} - \epsilon_{\min}, \quad \theta_P(\mathbf{x}) = -\phi(\mathbf{x}), \quad s_{xy} = \frac{1}{2}\epsilon_{yx},$$
$$s_{xy} = \frac{1}{2}\epsilon_{yx} \quad \Longrightarrow \quad \theta_R = s_{yx} - s_{xy}, \tag{A2}$$

where θ_P is the principle angle giving the orientation of the two principle axes of the strain matrix. Figure 9 illustrates $\gamma_{\max}$, s_{xy}, and s_{yx} at SP stacking for the experimental measurements and for the two models proposed in Refs. [5,10], showing that the experimental measurements are consistent with the model proposed in Ref. [5].

APPENDIX B: BRANCH POINTS

As discussed in Sec. II A, ζ_1 can be obtained by solving Eq. (35). The equation can be rewritten as

$$0 = f(\lambda,\ \zeta_1) = \zeta_1 + \lambda g(\zeta_1) \quad \text{with} \tag{B1}$$

$$g(\zeta_1) = \frac{\mathrm{d}}{\mathrm{d}\zeta_1}\left(\frac{c_2}{c_1}[J_1(3\zeta_1)]^2 + \sum_{n=-\infty}^{\infty}\left\{J_n(2\zeta_1)[J_{n+1}(\zeta_1)]^2 + \frac{c_3}{c_1}J_n(4\zeta_1)[J_{n+2}(2\zeta_1)]^2\right\}\right). \tag{B2}$$

In principle, for fixed λ, the nonlinear equation $f(\lambda, \zeta_1) = 0$ contains multiple solutions for ζ_1. The physical one is given by the solution that approaches 0 as $\lambda \to 0$ and therefore is well-defined at least for small λ. In addition, the solution contains branch points in the complex λ plane, whose magnitude gives the radius of convergence. Here, $g(\zeta_1)$ is a highly nonlinear function, and therefore, approximation methods are needed to derive the explicit expression of ζ_1 in terms of λ. The closed form of ζ_1 in Eq. (38) is obtained by expanding $g(\zeta_1)$ to the order of $O(\zeta_1^2)$, which works very well for real λ and real ζ_1. However, due to the different convergence behavior of $J_n(x)$ with the complex argument x, relatively larger errors are introduced for complex λ and thus for complex ζ_1. Consequently, Eq. (38) cannot provide precise values of the branch points and the resulting radius of convergence. In this section, we provide a different method to obtain the branch points without explicitly expressing ζ_1 in terms of λ.

Note that, at the branch points,

$$f(\lambda_{\mathrm{BP}},\ \zeta_{1,\mathrm{BP}}) = 0 \Longrightarrow \lambda_{\mathrm{BP}} = -\frac{\zeta_{1,\mathrm{BP}}}{g(\zeta_{1,\mathrm{BP}})}. \tag{B3}$$

Expanding the equation $f(\lambda, \zeta_1) = 0$ around the branch points $(\lambda_{\mathrm{BP}}, \zeta_{1,\mathrm{BP}})$, we obtain

$$\begin{aligned} 0 \approx\ & f(\lambda_{\mathrm{BP}},\ \zeta_{1,\mathrm{BP}}) + (\lambda - \lambda_{\mathrm{BP}})\,\partial_\lambda f(\lambda, \zeta_{1,\mathrm{BP}})|_{\lambda=\lambda_{\mathrm{BP}}} + (\zeta_1 - \zeta_{1,\mathrm{BP}})\,\partial_{\zeta_1} f(\lambda_{\mathrm{BP}}, \zeta_1)|_{\zeta_1=\zeta_{1,\mathrm{BP}}} \\ & + \tfrac{1}{2}\left[(\lambda-\lambda_{\mathrm{BP}})^2\partial_\lambda^2 + 2(\lambda-\lambda_{\mathrm{BP}})(\zeta_1-\zeta_{1,\mathrm{BP}})\partial_\lambda\partial_{\zeta_1} + (\zeta_1-\zeta_{1,\mathrm{BP}})^2\partial_{\zeta_1}^2\right] f(\lambda,\ \zeta_1)\big|_{\lambda=\lambda_{\mathrm{BP}},\zeta_1=\zeta_{1,\mathrm{BP}}} \\ & + O\left[(\lambda-\lambda_{\mathrm{BP}})^3, (\zeta_1-\zeta_{1,\mathrm{BP}})^3\right]. \end{aligned} \tag{B4}$$

Substituting $f(\lambda, \zeta_1) = \zeta_1 + \lambda g(\zeta_1)$ and $f(\lambda_{\mathrm{BP}},\ \zeta_{1,\mathrm{BP}}) = 0$ into the above equation, we find

$$\begin{aligned} 0 \approx\ & g(\zeta_{1,\mathrm{BP}})(\lambda-\lambda_{\mathrm{BP}}) + [1 + \lambda_{\mathrm{BP}} g'(\zeta_{1,\mathrm{BP}})](\zeta_1 - \zeta_{1,\mathrm{BP}}) \\ & + \tfrac{1}{2}[2(\lambda-\lambda_{\mathrm{BP}})(\zeta_1-\zeta_{1,\mathrm{BP}})g'(\zeta_{1,\mathrm{BP}}) + (\zeta_1-\zeta_{1,\mathrm{BP}})^2\lambda_{\mathrm{BP}} g''(\zeta_{1,\mathrm{BP}})], \end{aligned} \tag{B5}$$

which gives the approximate solution of ζ_1 when close to branch points. Around the branch points, ζ_1 cannot be uniquely solved; therefore,

$$1 + \lambda_{\mathrm{BP}} g'(\zeta_{1,\mathrm{BP}}) = 0 \quad \text{and} \quad g(\zeta_{1,\mathrm{BP}}) \neq 0 \quad \Longrightarrow \quad g(\zeta_{1,\mathrm{BP}}) - \zeta_{1,\mathrm{BP}} g'(\zeta_{1,\mathrm{BP}}) = 0 \quad \text{and} \quad g(\zeta_{1,\mathrm{BP}}) \neq 0\ ,$$

where in the last step, we substituted λ_{BP} from the relation $\zeta_{1,\mathrm{BP}} + \lambda_{\mathrm{BP}} g(\zeta_{1,\mathrm{BP}}) = 0$. Introducing

$$F(\zeta_1) = g(\zeta_1) - \zeta_1 g'(\zeta_1), \tag{B6}$$

with $g(\zeta_1)$ defined in Eq. (B2), the zero points of the function F give $\zeta_{1,\mathrm{BP}}$ at the branch points. Since the explicit formula of $g(\zeta_1)$ has already been given in Eq. (B2), $F(\zeta_1)$ can also be explicitly expressed as a nonlinear function. The numerical value of complex $\zeta_{1,\mathrm{BP}}$ can be accurately obtained by various numerical methods. Consequently, λ_{BP} can be obtained by Eq. (B3). Figure 10 shows two colored curves where the real part (in red) and the imaginary part (in blue) of F vanish, respectively, on the complex ζ_1 plane. The crossing points of these two colored curves give $\zeta_{1,\mathrm{BP}}$. As illustrated in the plot, the two crossing points are stable against any small change of the parameters in the function $f(\lambda, \zeta_1)$, and thus, the existence of these two branch points is robust.

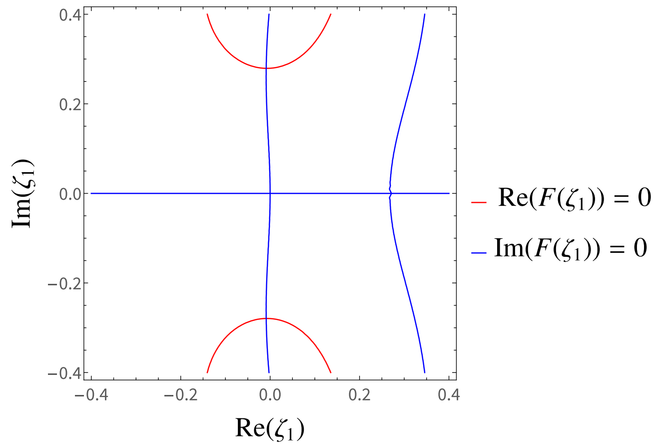

FIG. 10. The contour plot of (red) $\mathrm{Re}(F(\zeta_1)) = 0$ and (blue) $\mathrm{Im}[F(\zeta_1)] = 0$ on the complex ζ_1 plane, where $F(\zeta_1)$ is defined in Eq. (B6). The branch points $\lambda_{\rm BP}$ are given by Eq. (B3), where $\zeta_{1,c}$ is given by $F(\zeta_{1,c}) = 0$, the two intersection points of these two colored curves. Since these two points are the crossings, instead of the touching, of these two curves, the branch points are stable against any small perturbation of the parameters of Eq. (B2). The magnitude of $\lambda_{\rm BP}$ is the radius of convergence.

APPENDIX C: IMPROVEMENT OF THE ANALYTICAL FORMULA FOR UNSTRAINED LATTICE RELAXATION

In this section, we explicitly work out the improved formula for ζ_i ($i = 1$, 2, and 3) that works well for the twist angle $\theta > 0.4^\circ$. Note that the lattice relaxation can be approximated as

$$\delta\mathbf{U}(\mathbf{x}) \approx \frac{2}{|\mathbf{G}_1|^2}\sum_{a=1}^{3}\{\zeta_1\mathbf{G}_a\sin(\mathbf{g}_a\cdot\mathbf{x}) + \zeta_2(\mathbf{G}_a - \mathbf{G}_{a+1})\sin[(\mathbf{g}_a - \mathbf{g}_{a+1})\cdot\mathbf{x}] + 2\zeta_3\mathbf{G}_a\sin(2\mathbf{g}_a\cdot\mathbf{x})\}, \tag{C1}$$

where we have introduced the variables $\mathbf{g}_4 = \mathbf{g}_1$ and $\mathbf{G}_4 = \mathbf{G}_1$ for notational convenience. Correspondingly, the elastic energy can be simplified as

$$\frac{U_E}{A_{\rm tot}} = \text{const.} + \frac{3}{2}\mathcal{G}\theta^2\left(\zeta_1^2 + 9\zeta_2^2 + 16\zeta_3^2\right). \tag{C2}$$

As shown in Fig. 11, $|\zeta_{2,3}| \lesssim 0.1$ for twist angle $\theta > 0.4^\circ$. Therefore, the interlayer adhesion energy can be approximated as the following form:

$$\frac{U_B}{3c_1A_{\rm tot}} \approx F_1(\zeta_1) + [G_2(\zeta_1)\zeta_2 + G_3(\zeta_1)\zeta_3] + \left[H_{22}(\zeta_1)\zeta_2^2 + H_{23}(\zeta_1)\zeta_2\zeta_3 + H_{33}(\zeta_1)\zeta_3^2\right], \tag{C3}$$

where the cubic and higher-order terms of $\zeta_{2,3}$ are neglected. For the relaxation at the inner shell, we write $\zeta_1 = \zeta_1^{(0)} + \delta\zeta_1$, where $\zeta_1^{(0)}$ is given by Eq. (38). Full numerical calculation reveals $|\delta\zeta_1| < 0.05$ for $\theta > 0.4^\circ$. As a consequence, U_B can also be expanded up to the quadratic order of $\delta\zeta_1$, ζ_2, and ζ_3. By minimizing the total energy $U_E + U_B$, we obtain the linear equation for these three unknown variables and thus, in principle, can write their closed forms.

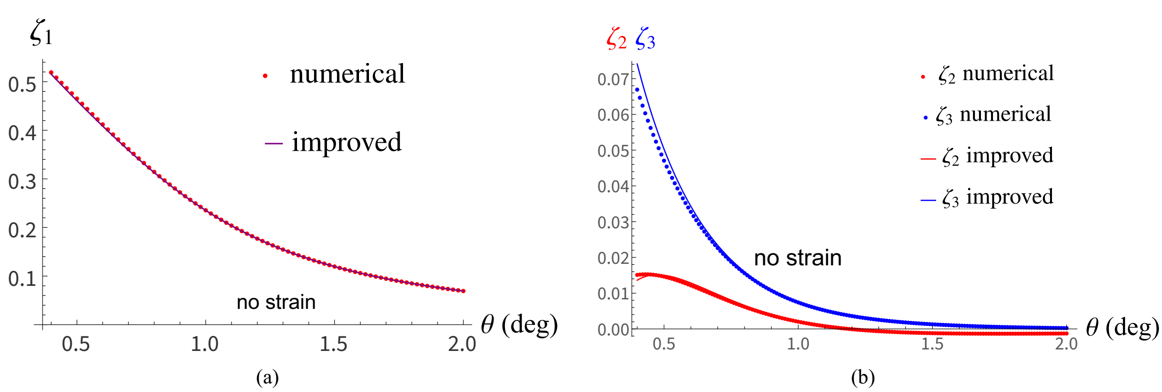

FIG. 11. Like Fig. 4, (left) ζ_1, (right red) ζ_2, and (right blue) ζ_3 for the lattice relaxation on the innermost, second, and third shells in the absence of external heterostrain. Dots are the solutions obtained by numerically solving Eq. (20). The colored curves are the solutions obtained by solving 3×3 matrix equation in Eq. (C12), which are much more complicated but also more accurate than Eqs. (38), (40), and (41).

Expanding $F(\zeta_1)$ to the order of ζ_1^5, G_i to the order of ζ_1^4, and H_{ij} to the order of ζ_1^3, we obtain

$$F_1(\zeta_1) \approx \left(-\zeta_1 + \frac{\zeta_1^2}{4} + \zeta_1^3 - \frac{3}{16}\zeta_1^4 - \frac{79}{192}\zeta_1^5\right) + \frac{c_2}{c_1}\left(\frac{9}{4}\zeta_1^2 - \frac{81}{16}\zeta_1^4\right) + \frac{c_3}{c_1}\left(2\zeta_1^2 - 2\zeta_1^3 - \frac{77}{12}\zeta_1^4\right), \tag{C4}$$

$$G_2(\zeta_1) \approx \left(-\frac{3}{2}\zeta_1 + \frac{3}{2}\zeta_1^2 + \frac{21}{16}\zeta_1^3 - \frac{19}{16}\zeta_1^4\right) + \frac{c_2}{c_1}\left(-3 + \frac{27}{2}\zeta_1^2 - \frac{27}{4}\zeta_1^3\right) + \frac{c_3}{c_1}\left(6\zeta_1 + 12\zeta_1^2 - 33\zeta_1^3\right), \tag{C5}$$

$$G_3(\zeta_1) \approx \left(-2\zeta_1 + \frac{17}{12}\zeta_1^3 - \frac{11}{48}\zeta_1^4\right) + \frac{c_2}{c_1}\frac{27}{2}\zeta_1^2 + \frac{c_3}{c_1}\left(-4 + 22\zeta_1^2 - 8\zeta_1^3\right), \tag{C6}$$

$$H_{22}(\zeta_1) \approx \left(\frac{9}{2}\zeta_1 - \frac{9}{16}\zeta_1^2 - \frac{153}{32}\zeta_1^3\right) + \frac{c_2}{c_1}\left(\frac{9}{4} - \frac{243}{8}\zeta_1^2 - \frac{405}{16}\zeta_1^3\right) + \frac{c_3}{c_1}\left(18\zeta_1 - \frac{45}{2}\zeta_1^2 - 36\zeta_1^3\right), \tag{C7}$$

$$H_{23}(\zeta_1) \approx \left(\frac{9}{2}\zeta_1 + \frac{3}{2}\zeta_1^2 - 7\zeta_1^3\right) + \frac{c_2}{c_1}\left(27\zeta_1 - \frac{81}{4}\zeta_1^2 - \frac{1215}{16}\zeta_1^3\right) + \frac{c_3}{c_1}\left(12\zeta_1 - 48\zeta_1^2 - 88\zeta_1^3\right), \tag{C8}$$

$$H_{33}(\zeta_1) \approx \left(7\zeta_1 - \frac{1}{4}\zeta_1^2 - \frac{35}{6}\zeta_1^3\right) - \frac{c_2}{c_1}\frac{81}{4}\zeta_1^2 + \frac{c_3}{c_1}\left(4 - 56\zeta_1^2\right). \tag{C9}$$

Note that $\zeta_1^{(0)}$ is the one that minimizes the total energy $U_E + U_B^{(0)}$, in which

$$\frac{U_B^{(0)}}{3c_1A_{\text{tot}}} = F_0(\zeta_1) = -\zeta_1 + \frac{\zeta_1^2}{4} + \zeta_1^3 + \frac{c_2}{c_1}\frac{9}{4}\zeta_1^2 + \frac{c_3}{c_1}2\zeta_1^2. \tag{C10}$$

We also define

$$\delta F(\zeta_1) = F_1(\zeta_1) - F_0(\zeta_1) = -\frac{3}{16}\zeta_1^4 - \frac{79}{192}\zeta_1^5 - \frac{c_2}{c_1}\frac{81}{16}\zeta_1^4 - \frac{c_3}{c_1}\left(2\zeta_1^3 + \frac{77}{12}\zeta_1^4\right). \tag{C11}$$

Now we are ready to write the matrix equation for $\delta\zeta_1$, ζ_2, and ζ_3

$$\begin{pmatrix} F_1''\big(\zeta_1^{(0)}\big) + \lambda^{-1} & G_2'\big(\zeta_1^{(0)}\big) & G_3'\big(\zeta_1^{(0)}\big) \\ G_2'\big(\zeta_1^{(0)}\big) & 2H_{22}\big(\zeta_1^{(0)}\big) + 9\lambda^{-1} & H_{23}\big(\zeta_1^{(0)}\big) \\ G_3'\big(\zeta_1^{(0)}\big) & H_{23}\big(\zeta_1^{(0)}\big) & 2H_{33}\big(\zeta_1^{(0)}\big) + 16\lambda^{-1} \end{pmatrix} \begin{pmatrix} \delta\zeta_1 \\ \zeta_2 \\ \zeta_3 \end{pmatrix} = -\begin{pmatrix} \delta F'\big(\zeta_1^{(0)}\big) \\ G_2\big(\zeta_1^{(0)}\big) \\ G_3\big(\zeta_1^{(0)}\big) \end{pmatrix}. \tag{C12}$$

Solving this matrix equation, we obtain the improved formula for ζ_1, ζ_2, and ζ_3, with their results plotted in Fig. 11.

APPENDIX D: IMPACT OF EXTERNAL HETEROSTRAIN

In this section, we derive the equation for $\delta\mathbf{W}_\mathbf{G}$, especially the expression of $B(\mathbf{G}, \{\mathbf{W}_{\mathbf{G}'}\})$ in Eq. (52). Notice that Eq. (20) is still valid in the presence of external heterostrain. As shown in Eqs. (47)–(50), the matrix $M_{\mu\nu}(\mathbf{g}_\mathbf{G}) = \sum_{i=0}^{2} M_\mathbf{G}^{(i)}$ is decomposed into the sum of three parts ordered by the powers of $\delta\mathbf{g}$ and gives the first term of Eq. (51). In addition, since $\delta\mathbf{U}(\mathbf{x}) = 2\sum_{\mathbf{G}\in\mathbb{H}} \mathbf{W}_\mathbf{G} \sin(\mathbf{g}_\mathbf{G}\cdot\mathbf{x})$, we have

$$\frac{\partial\delta U_\nu(\mathbf{x})}{\partial W_{\mathbf{G},\mu}} = 2\delta_{\mu\nu}\sin(\mathbf{g}_\mathbf{G}\cdot\mathbf{x}). \tag{D1}$$

The Fourier components of $\sin[\mathbf{G}'\cdot\mathbf{U}^-(\mathbf{x})]$ can be expressed as

$$\sin[\mathbf{G}'\cdot\mathbf{U}^-(\mathbf{x})] = \sum_\mathbf{g} f_{\mathbf{G}'}(\mathbf{g}, \{\mathbf{W}_\mathbf{G}\})\sin(\mathbf{g}\cdot\mathbf{x}) \quad\Longrightarrow\quad f_{\mathbf{G}'}(\mathbf{g}, \{\mathbf{W}_\mathbf{G}\}) = A_{\text{tot}}^{-1}\int d^2\mathbf{x}\ \sin[\mathbf{G}'\cdot\mathbf{U}^-(\mathbf{x})]\sin(\mathbf{g}\cdot\mathbf{x}). \tag{D2}$$

Then the right-hand side of Eq. (20) can be written as

$$\begin{aligned}\sum_{\mathbf{G}'} V_{\mathbf{G}'} f_{\mathbf{G}'}(\mathbf{g}_\mathbf{G}, \{\mathbf{W}\})G'_\mu &= \frac{1}{A_{\text{tot}}}\sum_{\mathbf{G}'} V_{\mathbf{G}'}\int d^2\mathbf{x}\ \sin[\mathbf{G}'\cdot\mathbf{U}^-(\mathbf{x})]\sin(\mathbf{g}_\mathbf{G}\cdot\mathbf{x})G'_\mu \\ &= -\frac{1}{2A_{\text{tot}}}\frac{\partial}{\partial W_{\mathbf{G},\mu}}\sum_{\mathbf{G}'} V_{\mathbf{G}'}\int d^2\mathbf{x}\ \cos[\mathbf{G}'\cdot\mathbf{U}^-(\mathbf{x})] = -\frac{1}{2}\frac{\partial}{\partial W_{\mathbf{G},\mu}}B(\mathbf{G}, \{\mathbf{W}\}),\end{aligned} \tag{D3}$$

where

$$\begin{aligned} B(\mathbf{G},\{\mathbf{W}\}) &= \frac{1}{A_{\text{tot}}}\int \mathrm{d}^2\mathbf{x}\ \cos[\mathbf{G}\cdot\mathbf{U}^-(\mathbf{x})] \\ &= \frac{1}{A_{\text{tot}}}\int \mathrm{d}^2\mathbf{x}\ \frac{1}{2}\left\{\exp(i\mathbf{g}_{\mathbf{G}}\cdot\mathbf{x})\exp\left[i\sum_{\mathbf{G}'\in\mathbb{H}} 2\mathbf{G}\cdot W_{\mathbf{G}'}\sin(\mathbf{g}_{\mathbf{G}'}\cdot\mathbf{x})\right]+\text{c.c.}\right\} \\ &= \frac{1}{A_{\text{tot}}}\int \mathrm{d}^2\mathbf{x}\ \exp(i\mathbf{g}_{\mathbf{G}}\cdot\mathbf{x})\prod_{\mathbf{G}'\in\mathbb{H}}\left[\sum_n J_n(2\mathbf{G}\cdot\mathbf{W}_{\mathbf{G}'})\exp(in\mathbf{g}_{\mathbf{G}'}\cdot\mathbf{x})\right]. \end{aligned} \tag{D4}$$

This gives the definition of $B(\mathbf{G},\{\mathbf{W}\})$, the same as Eq. (52).

As explained in the main text, $\mathbf{W}_{\mathbf{G}_a}$ can be approximately obtained by solving the matrix equation $(\mathcal{M}+\mathcal{T})_{a\mu,b\nu}\delta W_{\mathbf{G}_b,\nu} = -u_{a\mu}$, where the $\mathcal{M}$ matrix is given by Eq. (47). At large twist angle $\theta \gtrsim 1.4^\circ$, $\lambda \approx \zeta_1 \lesssim 0.1$, and thus, we can neglect the $\mathcal{T}$ matrix. For other cases, especially when $\theta \lesssim 1^\circ$, λ becomes sizable, and thus, we achieve a higher accuracy when we do not neglect the $\mathcal{T}$ matrix. We thus expand the inverse matrix using the power series in $\mathcal{T}$

$$(\mathcal{M}+\mathcal{T})^{-1} = \mathcal{M}^{-1} - \mathcal{M}^{-1}\mathcal{T}\mathcal{M}^{-1} + \mathcal{M}^{-1}\mathcal{T}\mathcal{M}^{-1}\mathcal{T}\mathcal{M}^{-1} + O(\mathcal{T}^3). \tag{D5}$$

where the obtained $\delta\mathbf{W}$ at different truncation orders are illustrated in Fig. 8 for $\theta = 1.05^\circ$ and Fig. 7 for $\theta = 1.4^\circ$.

1. Dominance of the first shell for the heterostrained lattice relaxation

In this subsection, we focus on the estimates of $\delta\mathbf{W}_{\mathbf{G}}$ with small strain. We will argue that $\delta\mathbf{W}_{\mathbf{G}}$ for $\mathbf{G}$ on the first shell is much larger than other $\delta\mathbf{W}_{\mathbf{G}}$s. For notational convenience, we introduce the variable

$$\epsilon_{\max} = \max(|\epsilon_1|,\ |\epsilon_2|) \quad\Longrightarrow\quad |\delta\mathbf{g}| \sim \epsilon_{\max}|\mathbf{G}|. \tag{D6}$$

When strain is small, $\epsilon_{\max} \ll \theta$, and thus, $|\delta\mathbf{g}_{\mathbf{G}}| \ll |\mathbf{g}_{\mathbf{G}}^{(0)}|$. Also, we generalize the variable $u_{a\mu}$ introduced in Eq. (56) as

$$u_{\mathbf{G},\mu} = \sum_\nu \big[M_{\mathbf{G}}^{(1)} + M_{\mathbf{G}}^{(2)}\big]_{\mu\nu} W_{\mathbf{G},\nu}^{(0)}, \tag{D7}$$

with the subscript $\mathbf{G}$ for all reciprocal lattice vectors. Consequently, δW can be written in the form of

$$\delta W_{\mathbf{G},\mu} = -\sum_{\mathbf{G}',\nu}(M+T)^{-1}_{\mathbf{G},\mu,\mathbf{G}',\nu}u_{\mathbf{G}',\nu}. \tag{D8}$$

As the first step, we estimate the magnitude of each term in Eq. (D8). From Eqs. (47)–(50), and note that $\mathcal{K}\sim\mathcal{G}$, it is found

$$\big|M^{(0)}_{\mathbf{G}\mu,\mathbf{G}\nu}\big| \sim \mathcal{G}\big|\mathbf{g}_{\mathbf{G}}^{(0)}\big|^2 \sim \mathcal{G}\theta^2|\mathbf{G}|^2, \quad \big|M^{(1)}_{\mathbf{G}\mu,\mathbf{G}\nu}\big| \sim \mathcal{G}|\delta\mathbf{g}_{\mathbf{G}}|\big|\mathbf{g}_{\mathbf{G}}^{(0)}\big| \sim \mathcal{G}\epsilon_{\max}\theta|\mathbf{G}|^2, \quad \big|M^{(2)}_{\mathbf{G}\mu,\mathbf{G}\nu}\big| \sim \mathcal{G}\epsilon_{\max}^2|\mathbf{G}|^2. \tag{D9}$$

As a consequence, for small strain,

$$\big|M^{(2)}_{\mathbf{G}\mu,\mathbf{G}\nu}\big| \ll \big|M^{(1)}_{\mathbf{G}\mu,\mathbf{G}\nu}\big| \ll \big|M^{(0)}_{\mathbf{G}\mu,\mathbf{G}\nu}\big| \quad\Longrightarrow\quad |M_{\mathbf{G}\mu,\mathbf{G}\nu}| \sim \big|M^{(0)}_{\mathbf{G}\mu,\mathbf{G}\nu}\big| \sim \mathcal{G}\theta^2|\mathbf{G}|^2. \tag{D10}$$

On the other hand, the upper bound of the T matrix elements can be estimated as

$$|T_{\mathbf{G}\mu,\mathbf{G}'\nu}| \lesssim c_1|\mathbf{G}_1|^2 = \lambda\mathcal{G}\theta^2|\mathbf{G}_1|^2. \tag{D11}$$

Clearly, when $\lambda \ll 1$, the above T matrix elements are much smaller than the magnitude of the M matrix elements, leading to the expansion of $(M+T)^{-1}$

$$(M+T)^{-1} \sim M^{-1} - M^{-1}TM^{-1} + O(T^2). \tag{D12}$$

In addition, due to the hierarchy structure of $M^{(0,1,2)}$ in Eq. (D10), for $\mathbf{G}$ at the jth shell,

$$|u_{\mathbf{G}\mu}| \sim \big|\big[M_{\mathbf{G}}^{(1)}\big]_{\mu\nu}W^{(0)}_{\mathbf{G}\nu}\big| \sim \mathcal{G}\epsilon_{\max}\theta|\mathbf{G}|^2\big|\mathbf{W}_{\mathbf{G}}^{(0)}\big| \sim \frac{\mathcal{G}\epsilon_{\max}\theta|\zeta_j||\mathbf{G}|^3}{|\mathbf{G}_1|^2}, \tag{D13}$$

where Eq. (46) is used in the last step.

As a result, $\{\mathbf{u}_{\mathbf{G}}\}$ obtains the same hierarchy structure as ζ_j for the unstrained lattice relaxation. Especially $|\mathbf{u}_{\mathbf{G}_a}|$ (for $a = 1$, 2, and 3) are much larger than other $\mathbf{u}_{\mathbf{G}}$ on outer $\mathbf{G}$-shells. Thus, for $\mathbf{G}$ on the first shell,

$$|\delta W_{\mathbf{G}_a\mu}| \sim (M^{-1})_{\mathbf{G}_a\mu,\mathbf{G}_a\nu}|u_{\mathbf{G}_a\nu}| \sim \frac{\epsilon_{\max}\zeta_1}{\theta|\mathbf{G}_1|}. \tag{D14}$$

For $\mathbf{G}$ on the jth $\mathbf{G}$-shell with $j > 1$, using Eq. (D12), we obtain

$$\delta W_{\mathbf{G},\mu} \approx -(M^{-1})_{\mathbf{G}\mu,\mathbf{G}\nu} u_{\mathbf{G}\nu} + \sum_{a=1}^{3}\sum_{\nu\rho\sigma}(M^{-1})_{\mathbf{G}\mu,\mathbf{G}\nu} T_{\mathbf{G}\nu,\mathbf{G}_a\rho}(M^{-1})_{\mathbf{G}_a\rho,\mathbf{G}_a\sigma} u_{\mathbf{G}_a\sigma}, \tag{D15}$$

where ν, ρ, and σ are in-plane spatial indices. Combining Eqs. (D9), (D11), and (D13), and noticing $|\mathbf{G}| \sim |\mathbf{G}_1|$ for $\mathbf{G}$ at the first several momentum shells, we conclude that

$$|(M^{-1})_{\mathbf{G}\mu,\mathbf{G}\nu}\mathbf{u}_{\mathbf{G}\nu}| \sim \frac{\epsilon_{\max}\zeta_j}{\theta|\mathbf{G}_1|}, \tag{D16}$$

$$|(M^{-1})_{\mathbf{G}\mu,\mathbf{G}\nu} T_{\mathbf{G}\nu,\mathbf{G}'\rho}(M^{-1})_{\mathbf{G}'\rho,\mathbf{G}'\sigma}\mathbf{u}_{\mathbf{G}'\sigma}| \sim \lambda\frac{\epsilon_{\max}\zeta_1}{\theta|\mathbf{G}_1|} \quad\Longrightarrow\quad |\delta W_{\mathbf{G},\mu}| \sim \frac{\epsilon_{\max}}{\theta|\mathbf{G}_1|}\max\left(|\zeta_j|,\ \lambda\zeta_1\right). \tag{D17}$$

Because of the hierarchy structure of ζ_j for the unstrained case, and $|\zeta_1| \sim \lambda \ll 1$, $\delta\mathbf{W}_{\mathbf{G}_a}$ estimated in Eq. (D14) is found to be much larger than $\delta\mathbf{W}$ of the outer shell estimated in Eq. (D17), allowing us to keep only $\delta\mathbf{W}_{\mathbf{G}_a}$ (with $a = 1$, 2, and 3) and obtaining Eq. (55).

APPENDIX E: SYMMETRY CONSTRAINTS

Most of the symmetries of the unstrained moire system, including the sixfold rotation C_{6z} along the $\hat{z}$ axis and mirror reflections along xz and yz planes, are broken by the presence of external heterostrain. Consequently, these transformations no longer impose constraints on the explicit form of the strained lattice relaxation but interestingly can still relate the lattice relaxations at different heterostrain orientations. Such relations play a crucial role in understanding the change of the electronic spectrum by strain, which we plan to address in upcoming papers. In this section, we will derive these relations.

As shown in Eq. (4), the heterostrain is described by three parameters: ϵ_1, ϵ_2, and ϕ. Therefore, in this subsection, the strain matrix is labeled as $S^\epsilon(\epsilon_1, \epsilon_2, \phi)$, and correspondingly, the reciprocal lattice vectors are labeled as

$$g_{\mathbf{G},\mu}(\epsilon_1, \epsilon_2, \phi) = [S^\epsilon(\epsilon_1, \epsilon_2, \phi) + i\theta\sigma^2]_{\mu\nu} G_\nu. \tag{E1}$$

Similarly, we label the lattice relaxation as $\delta\mathbf{U}(\mathbf{x}; \epsilon_1, \epsilon_2, \phi)$. Since $R(\phi) = -R(\phi + \pi)$, by the definition of S^ϵ in Eq. (4), $S^\epsilon(\epsilon_1, \epsilon_2, \phi) = S^\epsilon(\epsilon_1, \epsilon_2, \phi + \pi)$, implying that the strain matrix, and thus, the lattice relaxations $\delta\mathbf{U}$ are periodic functions of ϕ with the same periods of π. The same is true for $\mathbf{W}_\mathbf{G}$, the Fourier components of $\delta\mathbf{U}$,

$$\mathbf{W}_\mathbf{G}(\epsilon_1, \epsilon_2, \phi) = \mathbf{W}_\mathbf{G}(\epsilon_1, \epsilon_2, \phi + \pi). \tag{E2}$$

In addition, by Eq. (4),

$$S^\epsilon(\epsilon_1, \epsilon_2, \phi + \phi') = R^T(\phi')S^\epsilon(\epsilon_1, \epsilon_2, \phi)R(\phi'). \tag{E3}$$

Since $R(\phi) = \exp(-i\phi\sigma^2)$ and thus commutes with σ^2, Eq. (8) gives

$$g_{\mathbf{G},\mu}(\epsilon_1, \epsilon_2, \phi + \phi') = [R^T(\phi')]_{\mu\nu}\, g_{R(\phi')\mathbf{G},\nu}(\epsilon_1, \epsilon_2, \phi). \tag{E4}$$

The set of $\mathbf{G}$ vectors, which is unaffected by the heterostrain, is invariant under $C_{6z} = R(\pi/3)$. By setting $\phi' = \pi/3$ in the above formula, for two heterostrains $S^\epsilon(\epsilon_1, \epsilon_2, \phi)$ and $S^\epsilon(\epsilon_1, \epsilon_2, \phi + \pi/3)$, we conclude that the two sets of the corresponding moire reciprocal lattice vectors are related by C_{6z} rotation. Since $\mathbf{G}' \cdot \mathbf{U}^-(\mathbf{x}) = \mathbf{g}_{\mathbf{G}'} \cdot \mathbf{x} + \mathbf{G} \cdot \delta\mathbf{U}(\mathbf{x})$,

$$\begin{aligned}\mathbf{G}\cdot\mathbf{U}^-\left(\mathbf{x}; \epsilon_1, \epsilon_2, \phi + \frac{\pi}{3}\right) &= \mathbf{g}_\mathbf{G}\left(\epsilon_1, \epsilon_2, \phi + \frac{\pi}{3}\right)\cdot x + \mathbf{G}\cdot\delta\mathbf{U}\left(\mathbf{x}; \epsilon_1, \epsilon_2, \phi + \frac{\pi}{3}\right)\\ &= \mathbf{g}_{C_{6z}\mathbf{G}}(\epsilon_1, \epsilon_2, \phi)\cdot(C_{6z}\mathbf{x}) + (C_{6z}\mathbf{G})\cdot C_{6z}\delta\mathbf{U}\left(\mathbf{x}; \epsilon_1, \epsilon_2, \phi + \frac{\pi}{3}\right).\end{aligned} \tag{E5}$$

Since both the elastic energy U_E and the interlayer adhesion potential U_B are invariant under C_{6z}, we conclude

$$C_{6z}\delta\mathbf{U}\left(\mathbf{x}; \epsilon_1, \epsilon_2, \phi + \frac{\pi}{3}\right) = \delta\mathbf{U}(C_{6z}\mathbf{x}; \epsilon_1, \epsilon_2, \phi) \Longrightarrow \delta U_\mu\left(\mathbf{x}; \epsilon_1, \epsilon_2, \phi + \frac{\pi}{3}\right) = \left[R\left(\frac{\pi}{3}\right)\right]_{\nu\mu}\delta U_\nu\left[R\left(\frac{\pi}{3}\right)\mathbf{x}; \epsilon_1, \epsilon_2, \phi\right], \tag{E6}$$

leading to their corresponding Fourier components related by

$$W_{\mathbf{G},\mu}\left(\epsilon_1, \epsilon_2, \phi + \frac{\pi}{3}\right) = \left[R\left(\frac{\pi}{3}\right)\right]_{\nu\mu} W_{C_{6z}\mathbf{G},\nu}(\epsilon_1, \epsilon_2, \phi). \tag{E7}$$

For $\mathbf{G}$ at the innermost shell, we obtain

$$W_{\mathbf{G}_2,\mu}(\epsilon_1, \epsilon_2, \phi) = \left[R\left(\frac{2\pi}{3}\right)\right]_{\mu\nu} W_{\mathbf{G}_1,\nu}\left(\epsilon_1, \epsilon_2, \phi + \frac{2\pi}{3}\right), \tag{E8}$$

$$W_{\mathbf{G}_3,\mu}(\epsilon_1, \epsilon_2, \phi) = -\left[R\left(\frac{\pi}{3}\right)\right]_{\mu\nu} W_{\mathbf{G}_1,\nu}\left(\epsilon_1, \epsilon_2, \phi + \frac{\pi}{3}\right). \tag{E9}$$

Combining Eqs. (E2), (E8), and (E9), we conclude that $\mathbf{W}_{\mathbf{G}_1}(\epsilon_1, \epsilon_2, \phi)$ by varying ϕ from 0 to π already provides $\mathbf{W}_{\mathbf{G}_a}(\epsilon_1, \epsilon_2, \psi)$ ($a = 1$, 2, and 3) with arbitrary angle ψ.

In addition, the strain matrix also satisfies the relation

$$S^\epsilon\left(\epsilon_1, \epsilon_2, \frac{\pi}{2} - \phi\right) = \sigma^3 S^\epsilon(\epsilon_2, \epsilon_1, \phi)\sigma^3 = -\sigma^3 S^\epsilon(-\epsilon_2, -\epsilon_1, \phi)\sigma^3, \tag{E10}$$

$$\implies \quad g_{\mathbf{G},\mu}\left(\epsilon_1, \epsilon_2, \frac{\pi}{2} - \phi\right) = -\sigma^3_{\mu\nu} g_{\mathcal{R}_y\mathbf{G},\nu}(-\epsilon_2, -\epsilon_1, \phi) = \sigma^3_{\mu\nu} g_{-\mathcal{R}_y\mathbf{G},\nu}(-\epsilon_2, -\epsilon_1, \phi), \tag{E11}$$

where $\mathcal{R}_y$ is the mirror reflection along the xz plane that transforms an arbitrary in-plane vector $\mathbf{v}$ to $(\mathcal{R}_y\mathbf{v})_\mu = \sigma^3_{\mu\nu} v_\nu$. As shown in Fig. 3, the set of all $\mathbf{G}$ vectors is invariant under both $\mathcal{R}_y$ and $C_{2z}\mathcal{R}_y = -\mathcal{R}_y$. Thus, for two heterostrains described by $S^\epsilon(\epsilon_1, \epsilon_2, \frac{\pi}{2} - \phi)$ and $S^\epsilon(-\epsilon_2, -\epsilon_1, \phi)$, Eq. (E11) demonstrates that the two sets of the corresponding moire reciprocal lattice vectors are related by the mirror reflection $\mathcal{R}_y$. Notice that

$$\mathbf{g}_\mathbf{G}\left(\epsilon_1, \epsilon_2, \frac{\pi}{2} - \phi\right) + \mathbf{G}\cdot\delta\mathbf{U}\left(\mathbf{x}; \epsilon_1, \epsilon_2, \frac{\pi}{2} - \phi\right) = \mathbf{g}_{\mathcal{R}_y\mathbf{G}}(-\epsilon_2, -\epsilon_1, \phi)\cdot(-\mathcal{R}_y\mathbf{x}) + (\mathcal{R}_y\mathbf{G})\cdot\mathcal{R}_y\delta\mathbf{U}\left(\mathbf{x}; \epsilon_1, \epsilon_2, \frac{\pi}{2} - \phi\right). \tag{E12}$$

Since both U_E and U_B are invariant under $\mathcal{R}_y$, we conclude

$$\mathcal{R}_y\delta\mathbf{U}\left(\mathbf{x}; \epsilon_1, \epsilon_2, \frac{\pi}{2} - \phi\right) = \delta\mathbf{U}(-\mathcal{R}_y\mathbf{x}; -\epsilon_2, -\epsilon_1, \phi) \implies \delta U_\mu\left(\mathbf{x}; \epsilon_1, \epsilon_2, \frac{\pi}{2} - \phi\right) = \sigma^3_{\mu\nu}\delta U_\nu(-\mathcal{R}_y\mathbf{x}; -\epsilon_2, -\epsilon_1, \phi), \tag{E13}$$

and the corresponding Fourier components satisfy

$$W_{\mathbf{G},\mu}\left(\epsilon_1, \epsilon_2, \frac{\pi}{2} - \phi\right) = \sigma^3_{\mu\nu} W_{\mathcal{R}_y\mathbf{G},\nu}(-\epsilon_2, -\epsilon_1, \phi). \tag{E14}$$

Although Eqs. (E6), (E7), (E13), and (E14) are derived with external heterostrain, they are also valid in the absence of heterostrain by setting $\epsilon_1 = \epsilon_2 = 0$. The obtained formulas give the constraints on $\delta\mathbf{U}$ and the corresponding Fourier components $\mathbf{W}$ for the unstrained system, as have been derived in Ref. [9].

[1] Y. Cao, V. Fatemi, A. Demir, S. Fang, S. L. Tomarken, J. Y. Luo, J. D. Sanchez-Yamagishi, K. Watanabe, T. Taniguchi, E. Kaxiras *et al.*, Correlated insulator behaviour at half-filling in magic-angle graphene superlattices, Nature (London) **556**, 80 (2018).

[2] Y. Cao, V. Fatemi, S. Fang, K. Watanabe, T. Taniguchi, E. Kaxiras, and P. Jarillo-Herrero, Unconventional superconductivity in magic-angle graphene superlattices, Nature (London) **556**, 43 (2018).

[3] R. Bistritzer and A. H. MacDonald, Moire bands in twisted double-layer graphene, Proc. Natl. Acad. Sci. USA **108**, 12233 (2011).

[4] S. Fang and E. Kaxiras, Electronic structure theory of weakly interacting bilayers, Phys. Rev. B **93**, 235153 (2016).

[5] S. Carr, D. Massatt, S. B. Torrisi, P. Cazeaux, M. Luskin, and E. Kaxiras, Relaxation and domain formation in incommensurate two-dimensional heterostructures, Phys. Rev. B **98**, 224102 (2018).

[6] M. Koshino, N. F. Q. Yuan, T. Koretsune, M. Ochi, K. Kuroki, and L. Fu, Maximally localized Wannier orbitals and the extended Hubbard model for twisted bilayer graphene, Phys. Rev. X **8**, 031087 (2018).

[7] Z. Bi, N. F. Q. Yuan, and L. Fu, Designing flat bands by strain, Phys. Rev. B **100**, 035448 (2019).

[8] J. Kang and O. Vafek, Symmetry, maximally localized Wannier states, and a low-energy model for twisted bilayer graphene narrow bands, Phys. Rev. X **8**, 031088 (2018).

[9] J. Kang and O. Vafek, Pseudomagnetic fields, particle-hole asymmetry, and microscopic effective continuum Hamiltonians of twisted bilayer graphene, Phys. Rev. B **107**, 075408 (2023).

[10] N. N. T. Nam and M. Koshino, Lattice relaxation and energy band modulation in twisted bilayer graphene, Phys. Rev. B **96**, 075311 (2017); Erratum: Lattice relaxation and energy band modulation in twisted bilayer graphene [Phys. Rev. B **96**, 075311 (2017)], *ibid.* **101**, 099901(E) (2020).

[11] Y. H. Kwan, G. Wagner, T. Soejima, M. P. Zaletel, S. H. Simon, S. A. Parameswaran, and N. Bultinck, Kekulé spiral order at all nonzero integer fillings in twisted bilayer graphene, Phys. Rev. X **11**, 041063 (2021).

[12] D. E. Parker, T. Soejima, J. Hauschild, M. P. Zaletel, and N. Bultinck, Strain-induced quantum phase transitions in magic-angle graphene, Phys. Rev. Lett. **127**, 027601 (2021).

[13] X. Wang, J. Finney, A. L. Sharpe, L. K. Rodenbach, C. L. Hsueh, K. Watanabe, T. Taniguchi, M. A. Kastner, O. Vafek, and D. Goldhaber-Gordon, Unusual magnetotransport in twisted bilayer graphene from strain-induced open Fermi surfaces, Proc. Natl. Acad. Sci. USA **120**, e2307151120 (2023).

[14] L. Huder, A. Artaud, T. Le Quang, G. T. de Laissardière, A. G. M. Jansen, G. Lapertot, C. Chapelier, and V. T. Renard, Electronic spectrum of twisted graphene layers under heterostrain, Phys. Rev. Lett. **120**, 156405 (2018).

[15] A. Kerelsky, L. J. McGilly, D. M. Kennes, L. Xian, M. Yankowitz, S. Chen, K. Watanabe, T. Taniguchi, J. Hone, C. Dean *et al.*, Maximized electron interactions at the magic angle in twisted bilayer graphene, Nature (London) **572**, 95 (2019).

[16] Y. Xie, B. Lian, B. Jäck, X. Liu, C.-L. Chiu, K. Watanabe, T. Taniguchi, B. A. Bernevig, and A. Yazdani, Spectroscopic signatures of many-body correlations in magic-angle twisted bilayer graphene, Nature (London) **572**, 101 (2019).

[17] D. Wong, K. P. Nuckolls, M. Oh, B. Lian, Y. Xie, S. Jeon, K. Watanabe, T. Taniguchi, B. A. Bernevig, and A. Yazdani, Cascade of electronic transitions in magic-angle twisted bilayer graphene, Nature (London) **582**, 198 (2020).

[18] N. P. Kazmierczak, M. Van Winkle, C. Ophus, K. C. Bustillo, S. Carr, H. G. Brown, J. Ciston, T. Taniguchi, K. Watanabe, and D. K. Bediako, Strain fields in twisted bilayer graphene, Nat. Mater. **20**, 956 (2021).

[19] M. M. Al Ezzi, G. N. Pallewela, C. De Beule, E. J. Mele, and S. Adam, Analytical model for atomic relaxation in twisted moiré materials, Phys. Rev. Lett. **133**, 266201 (2024).

[20] J. Kang, Numerical data for lattice relaxation, OSF (2025), https://osf.io/usvkc/.

[21] A. Sinner, P. A. Pantaleón, and F. Guinea, Strain-induced quasi-1D channels in twisted moiré lattices, Phys. Rev. Lett. **131**, 166402 (2023).

[22] F. Guinea and N. R. Walet, Continuum models for twisted bilayer graphene: Effect of lattice deformation and hopping parameters, Phys. Rev. B **99**, 205134 (2019).

[23] G. Cantele, D. Alfè, F. Conte, V. Cataudella, D. Ninno, and P. Lucignano, Structural relaxation and low-energy properties of twisted bilayer graphene, Phys. Rev. Res. **2**, 043127 (2020).

[24] N. Leconte, S. Javvaji, J. An, A. Samudrala, and J. Jung, Relaxation effects in twisted bilayer graphene: A multiscale approach, Phys. Rev. B **106**, 115410 (2022).

[25] F. Gargiulo and O. V. Yazyev, Structural and electronic transformation in low-angle twisted bilayer graphene, 2D Mater. **5**, 015019 (2018).

[26] P. Cazeaux, D. Clark, R. Engelke, P. Kim, and M. Luskin, Relaxation and domain wall structure of bilayer moiré systems, J. Elast. **154**, 443 (2023).

[27] J. Wang, A. Khosravi, A. Silva, M. Fabrizio, A. Vanossi, and E. Tosatti, Bending stiffness collapse, buckling, topological bands of freestanding twisted bilayer graphene, Phys. Rev. B **108**, L081407 (2023).

[28] H. Ochoa, Moiré-pattern fluctuations and electron-phason coupling in twisted bilayer graphene, Phys. Rev. B **100**, 155426 (2019).

[29] B. Xie and J. Liu, Lattice distortions, moiré phonons, and relaxed electronic band structures in magic-angle twisted bilayer graphene, Phys. Rev. B **108**, 094115 (2023).

[30] A. Ceferino and F. Guinea, Pseudomagnetic fields in fully relaxed twisted bilayer and trilayer graphene, 2D Mater. **11**, 035015 (2023).

[31] E. T. Whittaker and G. N. Watson, *A Course of Modern Analysis* (Cambridge University Press, Cambridge, 1996), pp. 91–94.

[32] J. Herzog-Arbeitman, J. Yu, D. Călugăru, H. Hu, N. Regnault, O. Vafek, J. Kang, and B. A. Bernevig, Heavy fermions as an efficient representation of atomistic strain and relaxation in twisted bilayer graphene, arXiv:2405.13880.

[33] J. Herzog-Arbeitman, D. Călugăru, H. Hu, J. Yu, N. Regnault, J. Kang, B. A. Bernevig, and O. Vafek, Kekulé spiral order from strained topological heavy fermions, arXiv:2502.08700.

[34] K. Uchida, S. Furuya, J.-I. Iwata, and A. Oshiyama, Atomic corrugation and electron localization due to moiré patterns in twisted bilayer graphenes, Phys. Rev. B **90**, 155451 (2014).